TOPICAL REVIEW • OPEN ACCESS

Interlayer excitons diffusion and transport in van der Waals heterostructures

View the article online for updates and enhancements.

You may also like

Topical Review

Interlayer excitons diffusion and transport in van der Waals heterostructures

Yingying Chen[1] , **Qiubao Lin**[1], **Haizhen Wang**[2] **and Dehui Li**[2,3,*]

[1] School of Science, Jimei University, Yinjiang Road 185, Xiamen 361021, People's Republic of China
[2] School of Optical and Electronic Information, Huazhong University of Science and Technology, Luoyu Road 1037, Wuhan 430074, People's Republic of China
[3] Wuhan National Laboratory for Optoelectronics, Huazhong University of Science and Technology, Luoyu Road 1037, Wuhan 430074, People's Republic of China

E-mail: dehuili@hust.edu.cn

CrossMark

Abstract

The assembly of monolayer transition metal dichalcogenides (TMDs) in van der Waals heterostructures yields the formation of spatially separated interlayer excitons (IXs) with large binding energies, long lifetimes, permanent dipole moments and valley-contrasting physics, providing a compelling platform for investigating and engineering spatiotemporal IX propagation with highly tunable dynamics. Further twisting the stacked TMD monolayers can create long-term periodic moiré patterns with spatially modified band structures and varying moiré potentials, featuring tailored traps that can induce strong correlations with density–dependent phase transitions to modulate the exciton transport. The rich exciton landscapes in TMD heterostructures, combined with advancements in valleytronics and twistronics, hold great promise for exploring exciton-integrated circuits base on manipulation of exciton diffusion and transport. In this Review, we provide a comprehensive overview of recent progress in understanding IXs and moiré excitons, with a specific focus on emerging exciton diffusion and transport in TMD heterostructures. We put emphasis on spatial manipulation of exciton flux through various methods, encompassing exciton density, dielectric environment, electric field and structure engineering, for precise control. This ability to manipulate exciton diffusion opens up new possibilities for interconverting optical communication and signal processing, paving the way for exciting applications in high-performance optoelectronics, such as excitonic devices, valleytronic transistors and photodetectors. We finally conclude this review by outlining perspectives and challenges in harnessing IX currents for next-generation optoelectronic applications.

---

* Author to whom any correspondence should be addressed.

1. Introduction

Monolayer transition metal dichalcogenides (TMDs) have emerged as promising candidates for the exploration of exciton diffusion and transport dynamics [1–9]. These two-dimensional (2D) atomically thin semiconductors, including the well-known MoS_2, WS_2, $MoSe_2$ and WSe_2, exhibit direct bandgaps and weak dielectric screening in the 2D environment, which enables the formation of tightly bounded excitons through strong Coulomb interactions [10–14]. As a result, monolayer TMDs host rich excitonic physics that govern their spatiotemporal propagation, showing large exciton binding energies up to hundreds of millielectronvolts (meV) that can withstand thermal fluctuations at room temperature [15–18]. Moreover, excitons can interact with other quasiparticles, resulting in the emergence of many-body excitonic complexes with highly tunable optical and electrical properties [19–22]. Besides, the significant band splitting due to strong spin-orbit coupling, along with broken inversion symmetry and preserved time-reversal symmetry, allows for the coupled spin–valley physics to engineer valley-polarized excitons, providing monolayer TMDs with valley degree of freedom to process, storage and transport information [23–25]. Therefore, the rich exciton landscapes in monolayer TMDs offer an appealing pathway towards realizing exciton flux and exploring diverse exciton diffusion dynamics.

Notably, monolayer TMDs can be vertically stacked or laterally stitched by the top–down (e.g. dry-transfer) and bottom–up (e.g. chemical vapor deposition) approaches to form van der Waals (vdW) heterostructures with designed functionalities [26–29]. In contrast to traditional II–VI and III–V quantum wells where the lattice mismatch induces inevitable distortion and defects due to the covalent bonds, the vdW integration of disparate 2D materials circumvents the lattice compatibility with unprecedented flexibility, creating a new quantum system to explore novel phenomena [30, 31]. By engineering the bandgap with a type II (staggered) band alignment, ultrafast interfacial carrier dynamics take the stage within 50 fs [32–35], facilitating photoexcited electrons and holes to transfer to opposite layers, forming interlayer excitons (IXs) in vertical heterostructures or charge transfer (CT) excitons in lateral heterostructures (figures 1(a) and (b)) [36–39]. The spatial separation of electrons and holes reduce their wavefunction overlap, leading to lifetimes several orders of magnitude longer than intralayer excitons [40–42]. Additionally, IXs exhibit permanent dipole moments that can further be tuned by external electric fields [43, 44], making them attractive for the realization of exciton-integrated circuits that bridge the optical signals with electrical generation of IX currents [45–47]. Furthermore, the introduction of interlayer twist angles creates periodic moiré patterns with varying moiré potentials, offering a new avenue for the exploration of moiré excitons [48–50]. The moiré potential can also be tuned by altering the twist angle or lattice mismatch, allowing for the trapping or de-trapping of IXs and further modifying the exciton transport dynamics [51, 52]. More importantly, these exciton states retain the optically addressable spin–valley physics of constituent monolayers, endowing IXs with valley-dependent optical selection rules and valley Hall effects (VHEs) (figure 1(c)) [53–56], thereby generating valley-polarized IX flux under the circularly polarized excitation [57]. Therefore, TMD heterostructures hold great promise for investigating and engineering the transport dynamics of various exciton states, featuring interlayer, CT, and moiré excitons, opening novel avenues in the optoelectronics, twistronics and valleytronics, and pursuing towards the exploration of next-generation exciton-integrated circuits.

Several recent reviews have covered the exciton transport dynamics, primarily focusing on monolayer TMDs [58–60]. Although the exciton transport in monolayer TMDs exhibits unique behaviors, such as the halo effect [8], their tunability is usually constrained. For instance, the electrical control of neutral intralayer exciton transport remains challenging due to the in-plane dipole moment and charge neutrality. In contrast, IXs in separated layers exhibit prolonged lifetimes and out-of-plane dipole moments, which facilitate long-range transport and highly tunable diffusion dynamics. Therefore, beyond studying the underlying characteristics of the rich exciton landscapes in monolayer TMD and heterostructures, we provide an overview of the recent advancements in the spatiotemporal IX diffusion and transport dynamics in the TMD heterostructures, along with the manipulation of exciton flux and the associated practical applications. In this review, we begin with an introduction of fundamental properties of IXs and moiré excitons, outlining the optical signatures of exciton emission under varying excitation densities and electrical control in section 2. We then review state-of-the-art characterizations of spatial IX transport utilizing the 2D drift-diffusion model in section 3, including the stead-state acquirement under continuous wave excitation and the temporal record under the pulsed laser excitation, which shows long-range propagation distance that can be characterized by the exciton density and repulsive dipolar interactions. We also touch on the dynamics of moiré exciton diffusion by varying potential landscapes via twist angle, exciton density and temperature. Section 4 further highlights the manipulation of IX propagation by varying the exciton density to alter exciton phase, surrounding dielectric environment, electrical control and customized structure incorporation. Thereafter, the relevant applications in molding exciton transport, such as excitonic devices, valleytronic transistors and photodetectors are summarized in section 5. A final discussion with challenges and opportunities in controlling IX expansion and exploring the exciton-integrated circuits are presented in section 6.
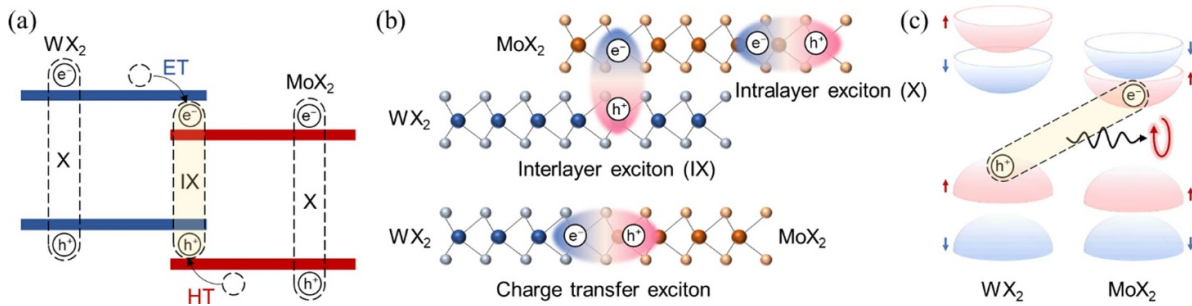
Figure 1. IXs in TMD heterostructures. (a) Schematic diagram of the typical type II MoX_2/WX_2 heterostructure and the charge transfer process. ET and HT stand for electron transfer and hole transfer, respectively. (b) Schematic illustrations of IXs in the vertical heterostructure and CT excitons in the lateral heterostructure. (c) Schematic description of valley-polarized IXs.

2. IX basics

2.1. IXs in TMD heterostructures

The vdW stacking of various TMD monolayers endows IXs with unique and intriguing properties compared to their monolayer counterparts, thereby attracting increasing attention in recent years. As previously mentioned, the rapid CT in the type II band alignment enables the formation of spatially indirect IXs [61], which can be experimentally observed in the photoluminescence (PL) measurements. As illustrated in figures 2(a) and (b), the first experimental observation of IXs was reported in a typical WSe$_2$/MoS$_2$ heterostructure. While the heterostructure region exhibit direct absorptions corresponding to monolayer WSe$_2$ and MoS$_2$, an additional peak appears at the lower energy side, along with the quenched emission of constituent monolayers, suggesting the presence of strong interlayer coupling and dominant IX emission within the TMD heterostructure [62]. Such IX emission has been widely documented in TMD heterostructures, with emission energies corresponding to the lowest-energy transitions of the type II band gap in the visible to near-infrared range [40, 62–73]. This IX formation can be further demonstrated by PL excitation (PLE) measurements [63, 66, 69]. As shown in figure 2(c), the PL intensity of IXs (blue dashed circle) enhanced only when the excitation energy resonates with intralayer exciton states of both layers by recording the PL intensity as a function of excitation energy, reinforcing the interlayer nature of IXs in TMD heterostructures.

Interestingly, the IX emission exhibits a strong dependence on the interlayer twist angle θ [65, 74–81]. The relative rotation between the hexagonal Brillouin zones of TMD monolayers can modify band structures in the heterostructure, significantly impacting both emission intensity and peak energy of IXs, and may also form moiré superlattices as discussed in the next section [48–50, 82, 83]. Typically, IX emission exhibits a maximum intensity at angles closet to 0° or 60°, and gradually become less apparent in the intermediate range of 10°–50°, indicating the change from momentum-direct to momentum-indirect IX states (figure 2(d)) [74]. Meanwhile, the twist angle (actually the interlayer distance) can modify the indirect band gap, making IXs to exhibit lowest peak energy at nearly 0°

or 60° alignment, with a gradual blueshift to a constant value for intermediate angles [75, 78–81]. Notably, although heterostructures with large twist angles show poor radiative emission, the interlayer coupling still cannot be ignored, evidenced by the strong PL quenching of intralayer excitons corresponding to monolayer TMDs in the heterostructure region and the presence of angle-independent sub-100 fs CT [76, 77], together with the nonradiative recombination of IXs with varied decay lifetimes without conclusive trend on the twist angle [77, 84].

Since IXs are spatially separated, with electrons and holes residing in different layers, the overlap of their wavefunctions is significantly reduced. This results in decreased exchange interactions and leads to long lifetimes of IXs that can extend to nanoseconds or even microseconds [40, 41, 63, 68, 85, 86]. As shown in figure 2(e), the time-resolved PL measurement have yielded an IX lifetime of 1.8 ns with a single exponential fitting [63]. This long lifetime highly surpasses the picosecond lifetime of intralayer excitons, making IXs more suitable for the practical applications of TMD-based excitonic devices with long-range exciton transport. More importantly, these aligned electron-hole pairs create permanent out-of-plane electrical dipole moments ($\boldsymbol{p} = edz$, where e is the charge quantity and d is the dipole size), enabling both optical and electrical control of the IX emission. As illustrated in figure 2(f), the peak energy of IXs exhibit a pronounced density–dependent blueshift with increasing excitation power, which is a hallmark of repulsive dipole–dipole interaction between IXs at high exciton density [66]. Besides, this energy shift can be quantitatively described by the capacitor model, $\Delta\mathcal{E} = nde^2/\varepsilon_{HS}\varepsilon_0$, where the n is the exciton density, ε_0 is the vacuum permittivity and ε_{HS} is the effective relative permittivity of the heterostructure [87, 88]. Furthermore, applying a vertical electric field $\boldsymbol{E}$ across the heterostructure can modify the energy landscape of IXs via the linear Stark effect $\Delta\mathcal{E} = -\boldsymbol{p} \cdot \boldsymbol{E}$ [43, 44, 89]. Generally, in a dual-gated device, the electric field can be independently controlled by adjusting the ratio of top and bottom gates (determined by the top and bottom hBN thickness) without changing the electrostatic doping of TMDs. As illustrated in figure 2(g), the peak energy of IXs linearly shift with variations in electric field, exhibiting blueshift (redshift) when then dipole moment is antiparallel
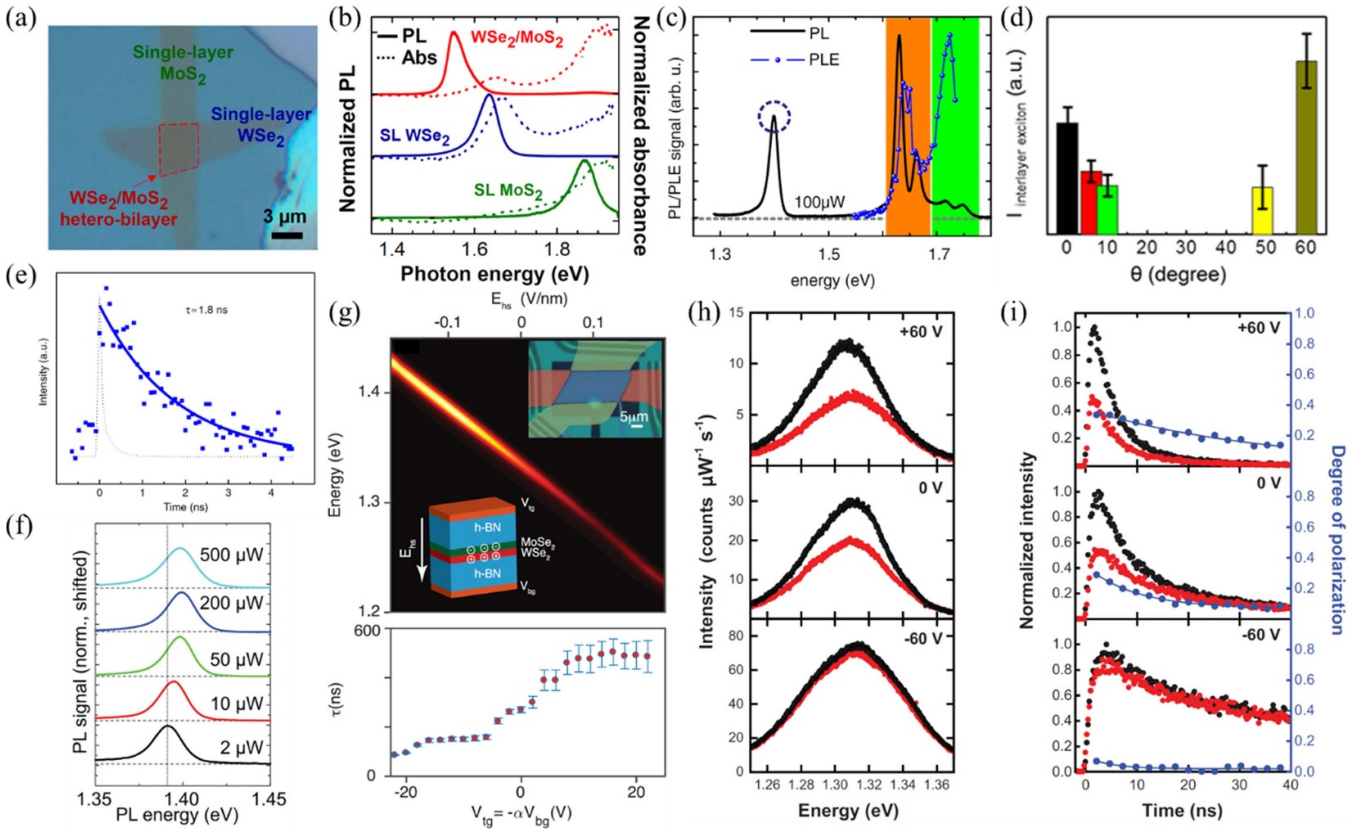
Figure 2. Fundamental properties of IXs in TMD heterostructures. Optical image (a) and normalized PL and absorption spectra (b) in the WSe$_2$/MoS$_2$ heterostructure. Scale bar, 3 μm. (a) And (b) Reproduced from [62]. CC BY 4.0. (c) PL and PLE spectra of the MoSe$_2$/WSe$_2$ heterostructure at 4.5 K. Reproduced from [66]. © IOP Publishing Ltd. All rights reserved. (d) PL peak intensity of IXs in the MoSe$_2$/WSe$_2$ heterostructure versus twist angle at room temperature. Reprinted (adapted) with permission from [74]. Copyright (2017) American Chemical Society. (e) Time-resolved PL spectrum of IXs in the MoSe$_2$/WSe$_2$ heterostructure at 20 K. The blue line shows the single exponential fit. Adapted from [63], with permission from Springer Nature. (f) Power-dependent PL spectra of the MoSe$_2$/WSe$_2$ heterostructure at 4.5 K. Reproduced from [66]. © IOP Publishing Ltd. All rights reserved. (g) PL spectra and lifetime of IXs as a function of vertical electric field in the MoSe$_2$/WSe$_2$ heterostructure at 4 K. Insets show the optical image and schematic illustration of the device. From [44]. Reprinted with permission from AAAS. Polarization-resolved (h) and time-resolved (i) PL spectra of IXs in the MoSe$_2$/WSe$_2$ heterostructure at 30 K under different gate voltages. The single exponential fits give out the valley polarization lifetimes of 39 $\pm$ 2, 10 $\pm$ 1, and 5 $\pm$ 2 ns for gate voltages of +60, 0, and −60 V, respectively. (h) And (i) From [54]. Reprinted with permission from AAAS.

(parallel) to the electric field [44]. Consequently, this linear slope enables the estimation of the dipole size, which has been found to be in the range of 0.5–0.9 nm [43, 90, 91]. Additionally, the electric field can also influence the IX lifetime by altering the overlap of electron and hole wavefunctions, thereby controlling the recombination rate. Specifically, a parallel electric field to IX diploe moment tends to separate IXs, thus reducing their recombination rate and lifetime.

Alternatively, varying the electrostatic doping level allows to further control over the conversion among complex exciton states. As doping level increases, singlet and triplet IXs become distinguishable [91, 92], and different charged states such as charged IXs or interlayer trions also emerge [93, 94]. With even higher exciton density, the strongly correlated many-body states should be further taken into consideration [95, 96]. Notably, electrostatic doping significantly affects the intervalley scattering, which in turn controls the valley polarization of IXs [97, 98], along with a tunable valley polarization lifetime (figures 2(h) and (i)) [54, 99]. Further considering

the opposite optical selection rules of singlet and triplet IXs [92, 100, 101], polarization switching devices can be achieved [91, 102, 103]. These phenomena demonstrate the highly tunable valley dynamics of IXs, showing promise for valleytronic applications based on IXs.

2.2. Moiré excitons in moiré superlattices

As stated above, stacking TMD monolayers with small twist angle θ and/or slight lattice mismatch δ can result in the formation of periodic moiré superlattices that can further extend to mesoscopic scale [104–110]. This periodicity is commonly referred to the moiré superlattice wavelength λ, which can be given by [48, 111]

$$\lambda = \frac{(1+\delta)\,a_0}{\sqrt{2\,(1+\delta)\,(1-\cos\theta)+\delta^2}} \tag{1}$$
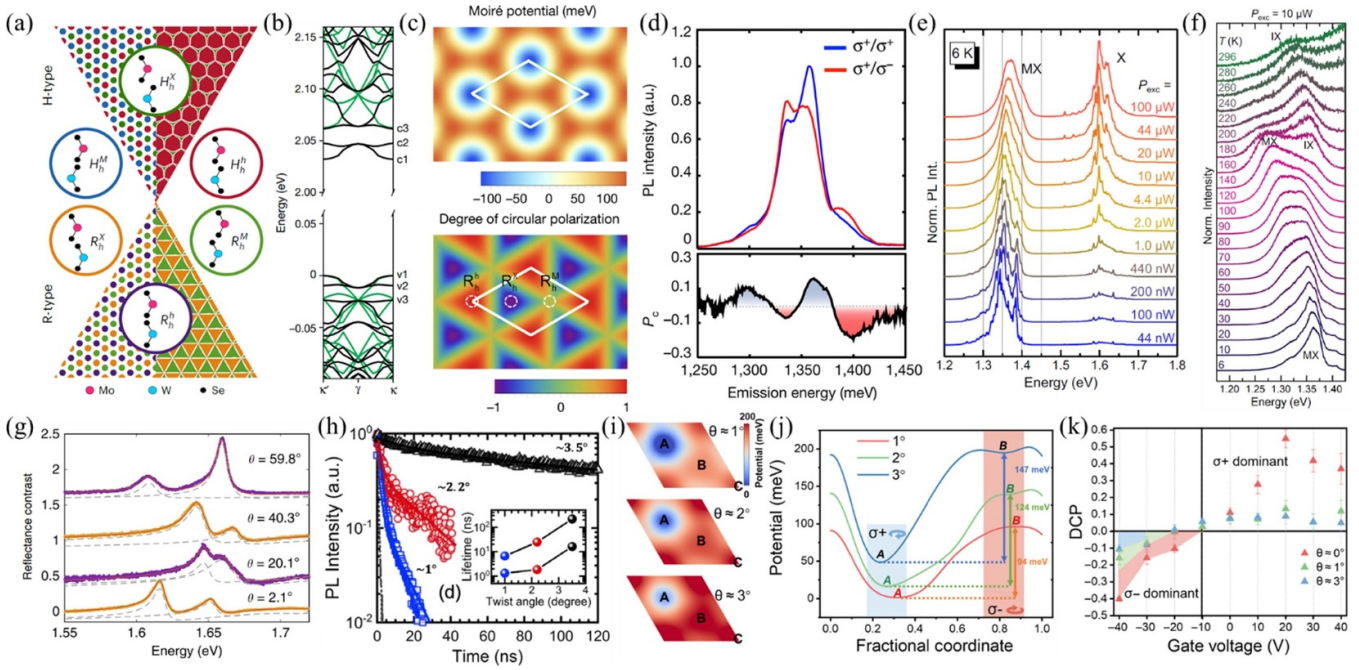
Figure 3. Basic characteristics of moiré excitons in moiré superlattices. (a) Schematic diagrams of R-type and H-type stacking moiré (left) and periodically reconstructed (right) patterns in the MoSe$_2$/WSe$_2$ heterostructure. Reproduced from [112]. CC BY 4.0. (b) Band structure of pristine WSe$_2$ (green line) and strained WSe$_2$ (black line) in the reconstructed WSe$_2$/WS$_2$ heterostructure. Adapted from [119], with permission from Springer Nature. (c) Spatial maps of moiré potential of IX transition and optical selection rules for K-valley IX excitons. (d) Circularly polarized PL spectra for σ^+ excitation of the MoSe$_2$/WSe$_2$ heterostructure with the twist angle of $1°$. (c) And (d) Adapted from [105], with permission from Springer Nature. Power—(e) and temperature—(f) dependent PL spectra of moiré excitons and free IXs in the WSe$_2$/MoSe$_2$ R-type stacking heterostructure. (e) And (f) Reproduced from [123]. CC BY 4.0. (g) Reflectance contrast spectra of hybrid moiré excitons in the WS$_2$/MoSe$_2$ heterostructure with different twist angles. Reproduced from [124]. CC BY 4.0. (h) Time-resolved PL spectra of IXs with different twist angles. The inset shows the twist-angle-dependent lifetimes in the MoSe$_2$/WSe$_2$ heterostructure, including both fast and slow decay components. Reprinted figure with permission from [125], Copyright (2021) by the American Physical Society. (i) Contour plots of stimulated moiré excitonic potentials for different twist angles. (j) Cross section of excitonic potentials at varying twist angles and the optical selection rules at different sites. (k) Twist-angle-dependent degree of polarization as a function of gate voltage of the WSe$_2$/WS$_2$ heterostructure. (i)–(k) From [126]. Reprinted with permission from AAAS.

where $\delta = |a_0' - a_0| / a_0$, a and a_0 are the lattice constants of the constituent monolayers. Typically, the size of the moiré period varies with twist angle, usually becoming larger with smaller twist angle, ranging from 1 to 100 nm [82, 83]. Besides, the symmetry of the moiré superlattice also depends on the twist angle. Given the three-fold rotational symmetry (C_3) in monolayer TMDs, they can be aligned nearly $0°$ or $60°$ to form rhombohedral (R-type) or hexagonal (H-type) stacking orders with three high-symmetry points (R_h^h, R_h^M, R_h^X or H_h^h, H_h^M, H_h^X) that preserving this C_3 symmetry (figure 3(a)) [105, 106, 112]. Here, the superscript refers to the hexagonal center (h), metal atom (M) or chalcogen atom (X) in the electron layer aligns vertically with the hexagonal center (h) in the hole layer marked by the subscript. These periodic local atomic registries significantly modulate the electronic band structure, leading to the formation of energy-separated flat minibands and spatially tailored moiré potentials (figures 3(b) and (c)) [109, 113, 114]. The moiré potential depths are reported to be on the order of tens to hundreds of meV based on first-principle calculations and scanning tunneling microscopy measurements [115–119]. Such deep potentials are expected to trap IXs in a quantum-dot-like manner, facilitating the discrete emission of

moiré excitons characterized by spectrally ultranarrow lines and imposing new optical selection rules at local potential minima [105, 110, 112, 120–122]. For instance, in the R-type stacking moiré pattern, the preservation of C_3 symmetry with different rotation centers allows exciton wave pockets at R_h^h (R_h^X) site to couple selectively to σ^+ (σ^-) circularly polarized light but is forbidden at R_h^M site, leading to the alternating circular polarization between ground- and excited-state IXs (figures 3(c) and (d)) [105]. Other work also reported a common interlayer atomic registry with C_3 symmetry in a given sample, revealing uniform circular polarization with same helicity in the R-type ($2°$) stacking bilayer but opposite helicity in the H-type ($57°$) stacking bilayer [110].

Interestingly, these sharp emission lines of moiré excitons usually appear at low excitation power [110, 112, 123, 127, 128]. As illustrated in figure 3(e), these disperse narrow peaks gradually blueshift and merge into broad IX emission with increasing incident power, suggesting the quantized filling of the moiré potential and promoting exciton delocalization [123, 127–129]. Such transition can be further corroborated by increasing temperature, which leads to the PL shift from moiré exciton to free IX dominated emission, demonstrating

excitons de-trapping from moiré potentials above at elevated temperatures (figure 3(f)) [123]. Conversely, a recent work further reports the existence of high-temperature moiré-locale excitons by enhancing the interlayer coupling and engineering the heterointerface [130]. These observations highlight the highly tunable exciton dynamics achieved by regulating the transition between localized and delocalized states in moiré potentials, which can impose a significant impact on the exciton transport behavior.

Notably, altering the twist angle hold great potential for excitonic manipulation within the moiré potentials [118, 124, 126, 131, 132]. Previous study has observed prominent multiple moiré exciton absorption peaks for near-zero twist angle but disappear for the twist angle larger than 3° [104]. Other work also reported robust interlayer and intralayer hybrid moiré excitons even for large twist angles, which show twist angle-dependent oscillator strengths, peak energies and dipole interactions (figure 3(g)) [124, 131, 133]. Moreover, the IX lifetime exhibits a strong dependence on the twist angle, with one order of magnitude enhancement as the twist angle increases from 1° to 3.5° due to the shift to momentum-indirect transition with increasing twist angle and extra relaxation channels for high-energy excited states within moiré potentials (figure 3(h)) [125]. Furthermore, the excitonic potential in moiré patterns varies with twist angle, showing deeper potential difference between site A (R_h^h) and site B (R_h^X) with increasing twist angle (figures 3(i) and (j)) [126]. Since electric control can effectively modulate the moiré potential and switch the local minimum from site A to site B [106, 134, 135], and site A (R_h^h) and site B (R_h^X) follow opposite optical selection rules, the twist angle-dependent polarization switching can be achieved (figure 3(k)). Besides, the electric control further promotes moiré excitons couple to charge carriers under electrostatic gating, forming moiré trions with different gating dependences and doping-dependent valley polarization [134, 136–138]. The twist-angle and electrically tunable emission of moiré excitons broadens the scope of excitonic physics, offering novel opportunities for excitonic manipulation and optoelectronic devices.

In this section, we have reviewed the fundamental properties of IXs and moiré excitons and their manipulation in TMD heterostructures. Due to their spatially indirect nature, IXs usually exhibit the lowest energy configuration, which can be clearly observed at low energy sides of the intralayer excitons in the PL spectra, and can be further verified by the PLE measurements. These spatially separated IXs not only display prolonged exciton lifetimes, but also possess permanent dipole moments that can be modified by the excitation power and electric field, holding great potentials for the exciton condensation and superfluidity. Further twisted TMD heterostructures with small twist angles and/or slight lattice mismatches can form periodic moiré superlattices, introducing new lattice length and moiré potentials, which offer a powerful platform to engineer the band structures and excitonic physics. The moiré-trapped IXs exhibit spectrally narrow bandwidths and new optical selection rules, which can be tuned by varying the

excitation power, temperature, and twist angles. Besides, the electric control can introduce multiple exciton complexes, significantly manipulating their lifetimes and valley polarization. The ability to control the formation, dynamics, and properties of IXs opens up new avenues for designing and optimizing excitonic systems, paving the way for future advances in optoelectronics and quantum technologies.

3. Characterization of IX diffusion and transport

3.1. Steady-state spatial characterization of IX diffusion and transport

The long lifetime of IXs enables them to travel long distances before recombination. While the local laser excitations create the concentration gradients to drive IXs diffusion in the heterostructure, the repulsive exciton–exciton interaction of IXs can act as a density–dependent drift force to enhance IX transport at high incident powers. In this case, the spatial and temporal distribution of exciton density $n(\mathbf{r}, t)$ can be described by the classical 2D drift-diffusion model [88, 139]:

$$\frac{\partial n(\mathbf{r}, t)}{\partial t} = D\nabla^2 n(\mathbf{r}, t) + \mu\nabla(n(\mathbf{r}, t)\nabla(\delta E(n(\mathbf{r}, t)))) - \frac{n(\mathbf{r}, t)}{\tau} + G \quad (2)$$

where μ is the exciton mobility, D is the exciton diffusion coefficient (or diffusivity) which can be expressed with μ and temperature T via the Einstein relation $D = \mu k_B T$, τ is the exciton lifetime, G is the exciton generation rate, and δE is the total potential energy including exciton–exciton repulsion and external potentials such as electric field. On the right-hand side of equation (2), the first term represents the diffusion term, the second term denotes the drift term and the third teem accounts for the population decay. In the absence of external fields, the equation (2) can be simplified to:

$$\frac{\partial n(\mathbf{r}, t)}{\partial t} = \nabla[D\nabla n(\mathbf{r}, t) + \mu n(\mathbf{r}, t)\nabla(u_0 n(\mathbf{r}, t))] - \frac{n(\mathbf{r}, t)}{\tau} + G \quad (3)$$

where u_0 is the exciton–exciton interaction energy. We should note that the drift term contributed from repulsive exciton–exciton interaction comprises two components: dipolar repulsion and exchange interaction. Since the electron-hole separation of IXs (0.5–0.9 nm) is comparable to the Bohr radius of IXs (1 nm), the exchange interaction can be negligible in certain cases to simplify the issue [140]. Therefore, only the repulsive dipole–dipole interactions are taken into consideration in TMD heterostructures. Notably, this dipolar repulsion can also be disregarded for exciton density lower than 10^{10} cm^{-2} [51, 90].

Under steady-state conditions without external potentials, the equation (3) exhibits an analytical solution:

$$n \propto \int_{-\infty}^{\infty} K_0 \left(\frac{r}{L_D} \right) \mathrm{e}^{-(r-r')^2/w^2} \mathrm{d}r' \tag{4}$$

where K_0 is the modified Bessel function, r is distance from the excitation spot, w is width of the laser spot, and L_D is diffusion length. In addition, the diffusion coefficient can be derived from the diffusion length and lifetime using the relation $D = \frac{L_D^2}{\tau}$.

In this scenario, a quantitative analysis of IX diffusion and transport can be performed. For instance, Jauregui *et al* have demonstrated the visible IX propagation controlled by the excitation power, observing PL signals beyond the diffraction limit of the focused laser beam (figure 4(a)) [44]. As the incident power increases, the exciton cloud exhibits a pronounced growing size limited in the heterostructure region, suggesting the increasing IX diffusion at elevated powers. The L_D can be quantified by fitting the radially averaged PL intensity away from the excitation spot with $\mathrm{e}^{-r/L_D}/\sqrt{r/L_D}$, revealing a nonlinear increasing trend (figure 4(b)). Since the time-resolve PL exhibits two decay components with lifetimes of $\tau_1 \sim 10$ ns and $\tau_2 \sim 100$ ns, the diffusion coefficient shows two variable ranges of 0.01–0.1 cm^2 s^{-1} and 0.1–1 cm^2 s^{-1}, representing the upper and lower limits for nonlinear IX diffusion process driven by the repulsive dipolar interaction. To mitigate the influence of moiré potentials on IX diffusion [51], Unuchek *et al* have inserted a monolayer hBN between WSe$_2$ and MoSe$_2$ to reduce the moiré interaction and Auger recombination to promote efficient exciton transport [90]. As shown in figure 4(c), the spatial PL emission profiles exhibit significant expansion with increasing excitation power compared to the device without hBN spacer. They defined the effective L_D as the distance at which the emission intensity decreases to $1/e$ as its initial value. This effective L_D demonstrates a linear dependence on excitation power, indicating the absence of exciton–exciton annihilation (EEA) and the dominance of exciton–exciton repulsion (figure 4(d)). Lately, Zhang *et al* reported an unusual correlation between L_D with excitation power when focusing only the regions far from the excitation spot [141]. They obtained a constant diffusion length of 17 ± 6 μm, which remains unchanged with excitation power variations due to dipolar repulsive interactions (figure 4(e)). In addition, regarding of the robust IX emission in monolayer WSe$_2$/2D perovskite heterostructure [142], Yao *et al* have demonstrated the large diffusion coefficient of IXs is about 10 cm^2 s^{-1}, which is at least an order magnitude larger than of IXs in previous TMD heterobilayers [143]. Interestingly, the diffusion length decreases with increasing power, which may be attributed to reduced IX lifetimes. The observed distinct diffusion behavior across different types of TMD-based heterostructures highlights the intriguing exciton dynamics under

various excitation power conditions, shedding light on understanding the fundamental mechanisms governing exciton diffusion, which has gathered significant research attention in recent years.

Very recently, Fowler-Gerace *et al* have revealed ultralong IX transport with $1/e$ decay distance surpassing 100 μm when the optical excitation is near resonant with the direct exciton energy of MoSe$_2$ or WSe$_2$, suggesting negligible emission decay within the heterostructure (figures 4(f) and (g)) [144]. This long-range IX transport only sustains at temperatures below 10 K and exhibits a non-monotonically dependence on excitation power (figure 4(h)). Specifically, the transport distance increases gradually with power, exceeding 100 μm with diffusivity reaching up to 10^4 cm^2 s^{-1}, before decreasing at higher powers. These observations cannot be explained by the classical transport model, but are consistent with the theoretical predictions of Bose–Hubbard model describing IX superfluidity and excitonic insulators [145, 146].

Moreover, since IXs sustain the spin–valley polarization with long valley lifetimes extending to nanosecond timescales, it is possible to observe valley polarized IX drift-diffusion under the circularly polarized excitation. Indeed, Rivera *et al* have reported the density–dependent spatial distribution of the valley-polarized IXs [54]. The spatial degree of polarization evolves into a ring-like pattern with increasing incident power, demonstrating the discrepant drift-diffusion of the σ^+ and σ^- component (figures 4(i) and (j)). The polarization ring may be attributed to the valley-dependent many-body interactions, where the majority valley excitons experience stronger exchange interactions and higher density gradients, leading to more rapid diffusion. Table 1 further summarizes the recently reported exciton diffusion in TMD heterostructures. These observations provide valuable insights into valley-polarized IX transport, potentially bridging a gap in the field of excitonic and valleytronic devices.

3.2. Spatiotemporal characterization of IX diffusion and transport

Beyond studies of the steady-state IX diffusion, the employment of temporal characterization enables the investigation of spatiotemporal IX diffusion dynamics under pulsed laser excitation. The long-lived IXs, along with the rapidly decaying direct intralayer excitons, allow them to diffuse away from the excitation spot after the pulse excitation, leading to a wider spatial distribution that can be detected at different time windows (figure 5(a)) [147]. Notably, by quickly scanning PL images across excitation spot at various times, Sun *et al* have observed a sublinear spatiotemporal expansion of the exciton cloud (figure 5(b)) [140]. They employed equation (3) to stimulate and fit the exciton area as a function of time under different diffusion coefficients, both with and without considering the exciton–exciton interaction strength U_{xx} (determined using the parallel-plate capacitor model, $U_{xx} = \frac{e^2 d}{\varepsilon_0 \varepsilon_{\mathrm{HS}}}$ [87]), demonstrating that repulsive dipolar interaction acts as the drift source controlling IX propagation (figures 5(c)
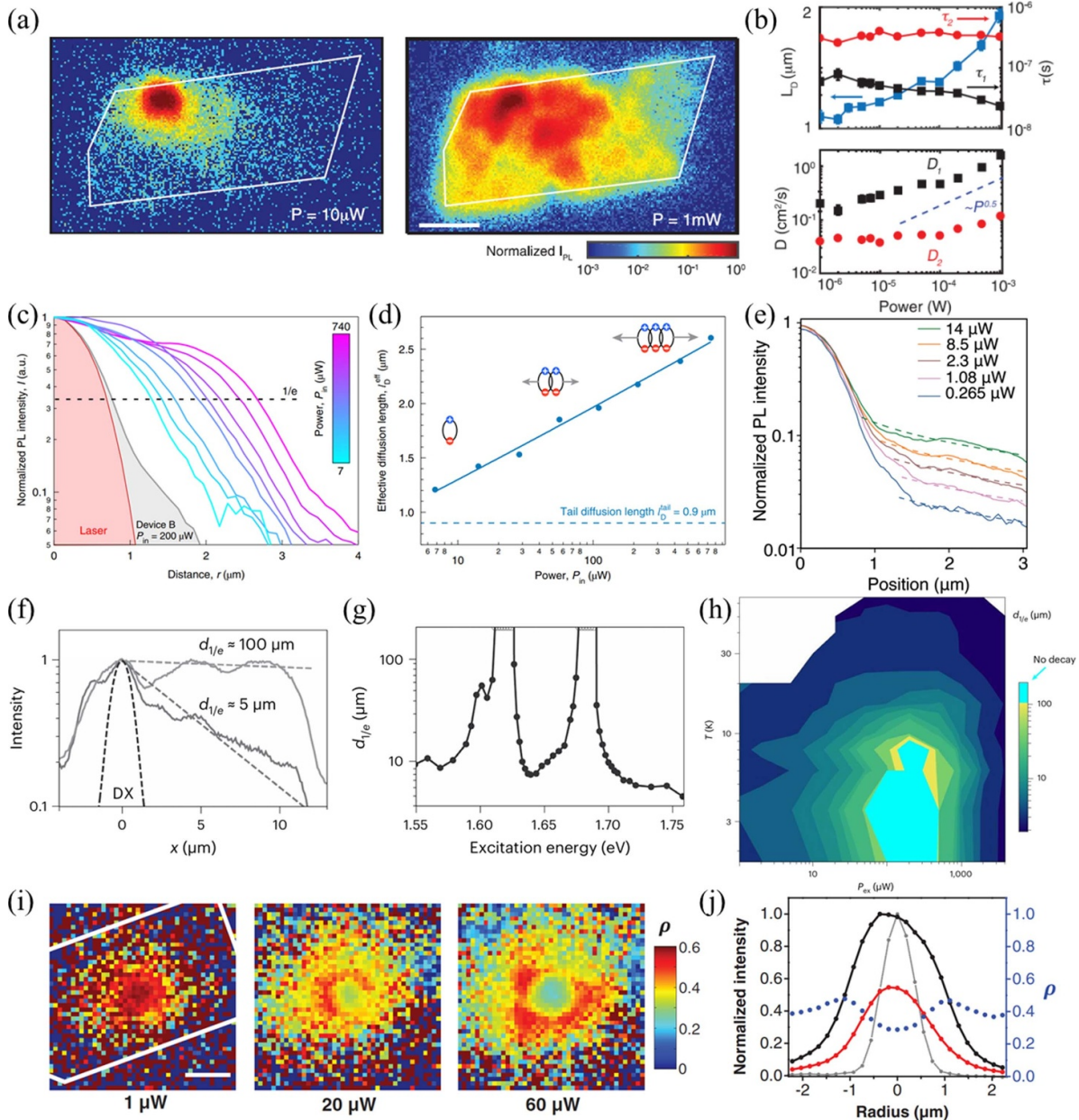
Figure 4. Steady-state characterization of IX diffusion and transport. (a) Spatial normalized PL with the excitation power of 10 μW and 1 mW in the MoSe$_2$/WSe$_2$ heterostructure, respectively. The white lines depict the heterostructure area. Scale bar, 5 μm. (b) L_D, τ, and D versus excitation power. (a) And (b) From [44]. Reprinted with permission from AAAS. (c) Power dependence of normalized profiles of PL intensity as a function of the distance from the excitation point in the WSe$_2$/hBN/MoSe$_2$ heterostructure. (d) Effective L_D as a function of excitation power. (c) And (d) Adapted from [90], with permission from Springer Nature. (e) Power dependence of radially averaged PL intensity of IXs as a function of the distance r in the MoSe$_2$/hBN/MoSe$_2$ heterostructure. Reprinted figure with permission from [141], Copyright (2024) by the American Physical Society. (f) Normalized IX PL profiles for laser excitation off (1.771 eV) and near (1.676 eV) resonant with the direct excitons in the MoSe$_2$/WSe$_2$ heterostructure. (g) The 1/e decay distances as a function of excitation energy. (h) Power and temperature dependence of 1/e decay distances. (f)–(h) Adapted from [144], with permission from Springer Nature. (i) Power-dependent spatial map of valley-polarized IXs in the MoSe$_2$/WSe$_2$ heterostructure. The white line outlines the heterostructure area. Scale bar, 2 μm. (j) Polarization-resolved spatial profiles of IXs under 40 μW excitation. (i) And (j) From [54]. Reprinted with permission from AAAS.

and (d)). While previous studies focused solely the dipolar repulsion, Erkensten *et al* have developed a comprehensive microscopic theory for IX transport that includes both repulsive exciton–exciton interaction and attractive exchange interaction (figure 5(e)), leading to the highly nonlinear IX migration [164].

In order to quantify the exciton diffusion at the initial time and any delay time t during the exciton trans-

Table 1. Summary of state-of-the-art IX propagation in TMD heterostructures.

Heterostructure	θ (°)	Exciton density (cm^{-2})	L_D (μm)	τ (ns)	D (cm^2 s^{-1})	Temperature (K)	References
MoSe$_2$/WSe$_2$	0	5×10^{11}	1–2	τ_1–10 τ_2–100	0.01–0.1 0.1–1	4	[44]
WSe$_2$/hBN/MoSe$_2$	0.3 ± 0.25	$<3 \times 10^{11}$	1.2–2.6	—	—	4	[90]
MoSe$_2$/hBN/MoSe$_2$	0	7.6×10^{10}–1.3×10^{11}	17 ± 6	—	—	6	[141]
1L-WSe$_2$/(iso-BA)$_2$PbI$_4$	—	—	4–7.6	3–9	$\sim$10	78	[143]
2L-WSe$_2$/(iso-BA)$_2$PbI$_4$			2.7–5.4	0.4–0.9			
MoSe$_2$/WSe$_2$	1.1	2×10^{11}	>100	$\sim$10	2×10^1–10^4	<10	[144]
MoSe$_2$/WSe$_2$	0	$\sim 10^{12}$–10^{13}	—	10	0.01	30	[54]
MoS$_2$/3L-hBN/MoS$_2$	—	—	1	10	1	300	[147]
WSe$_2$/hBN/MoSe$_2$	—	2×10^{11}–8×10^{11}	0.8–2	3.5	0.15	4.6	[140]
WS$_2$/PtSe$_2$	—	$<4 \times 10^{12}$	0.2	0.4	0.9 ± 0.2	Room temperature	[148]
WSe$_2$/MoSe$_2$	0	$\sim 10^9$	3–6 (2.4–13.5)	1.7 (1.8)	50–1506 (32–1013)	4	[51]
	1.1 ± 0.3		—	1	—		
	3.5 ± 0.3		0.35–1.1	100	0.012–0.12		
	53.9		—	—	0.11		
WSe$_2$/MoSe$_2$	2.49	$\sim 10^{12}$	—	—	0.09	296	[52]
	5.12		—	—	0.05		
WS$_2$/WSe$_2$	60	2.1×10^{11}–6×10^{11}	—	0.97 ± 0.18	5.4 ± 0.6	295	[149]
WSe$_2$/WSe$_2$	0	—	—	—	$\sim$2	80–400	[150]
WS$_2$/WSe$_2$	0 60	5×10^{10}	$\sim$0.6	$\sim$12	0.16 0.24	30	[151]
MoSe$_2$/WSe$_2$	2.6 ± 0.5	$>10^{12}$	$\sim$2	$\sim$20	$\sim$2	4	[152]
MoSe$_2$/WSe$_2$	1.3 ± 0.6	1.2×10^{11}	0.5	0.78 ± 0.1	1.1 ± 0.2	5	[153]
WS$_2$/WSe$_2$	0 ± 0.5	1.15×10^{12}	$\sim$1.1	9.5 ± 0.3	$\sim$0.7	83	[154]
WSe$_2$ homobilayer	0	$\sim 10^{12}$	—	0.4–0.75	0.32	4	[155]
MoS$_2$/WS$_2$	3.48	—	0.133	$\sim$1	0.2	—	[108]
MoSe$_2$/WSe$_2$	0.5 ± 0.8	2×10^{11}	13	1000	$\sim$1	<50	[156]
WSe$_2$ homobilayer	0	—	20	—	—	100	[157]
MoSe$_2$/WSe$_2$	54.4	—	10–20	—	—	10	[158]
MoS$_2$/WSe$_2$	0	—	3–5.5	—	—	Room temperature	[159]
WSe$_2$ homobilayer	0	—	4	4.18	—	10	[160]
WSe$_2$/MoSe$_2$	0	—	1.5–3	—	—	6	[161]
MoTe$_2$/MoS$_2$	0	8×10^{11}	1.1–3	—	—	5	[162]
MoSe$_2$/WSe$_2$	0	1–2.5×10^{12}	0.95–1.6	$\sim$1	—	4	[163]

port, the exciton density created by the Gaussian excitation beam is assumed to follows a Gaussian spatial distribution (figure 5(f)) [8, 164, 166–168]:

$$n(x,y,0) = N\exp\left[-\frac{(x-x_0)^2}{2\sigma_{x,0}^2} - \frac{(y-y_0)^2}{2\sigma_{y,0}^2}\right]$$

$$n(x,y,t) = N\exp\left[-\frac{(x-x_0)^2}{2\sigma_{x,t}^2} - \frac{(y-y_0)^2}{2\sigma_{y,t}^2}\right]. \quad (5)$$

Here, $n(x,y,0)$ is the initial exciton population, $n(x,y,t)$ is the exciton density as a function of position (x,y) and time t, N is a constant, $\sigma_{t,x}^2$ and $\sigma_{t,y}^2$ are the time-dependent variances of the Gaussian along x and y directions. For isotropic diffusion, $\sigma_{x,t} = \sigma_{x,t} = \sigma_t$. Therefore, the exciton diffusion length L_D and diffusion coefficient D can be given by:

$$\sigma_t^2 = \sigma_0^2 + L_D^2 = \sigma_0^2 + aDt \quad (6)$$

where a is a coefficient related to the diffusion dimensionality. The experimentally measured $\sigma_t^2 - \sigma_0^2$ corresponds to the mean squared distance travelled by excitons at a later delay time t. For 2D diffusion, $a = 4$. Therefore, the diffusion coefficient D is given by fitting the variance as a function of time:

$$D = \frac{\sigma_t^2 - \sigma_0^2}{4t}. \quad (7)$$

When $t = \tau$, the diffusion length L_D can be given by:

$$L_D = \sqrt{\sigma_t^2 - \sigma_0^2} = 2\sqrt{D\tau}. \quad (8)$$

In this scenario, exciton diffusion can also be described by the 2D drift-diffusion model, where the spatiotemporal distribution of exciton density adheres to equation (3). As illustrated in figure 5(g), while purely diffusive process exhibits a linear increase in variance over time, the presence of
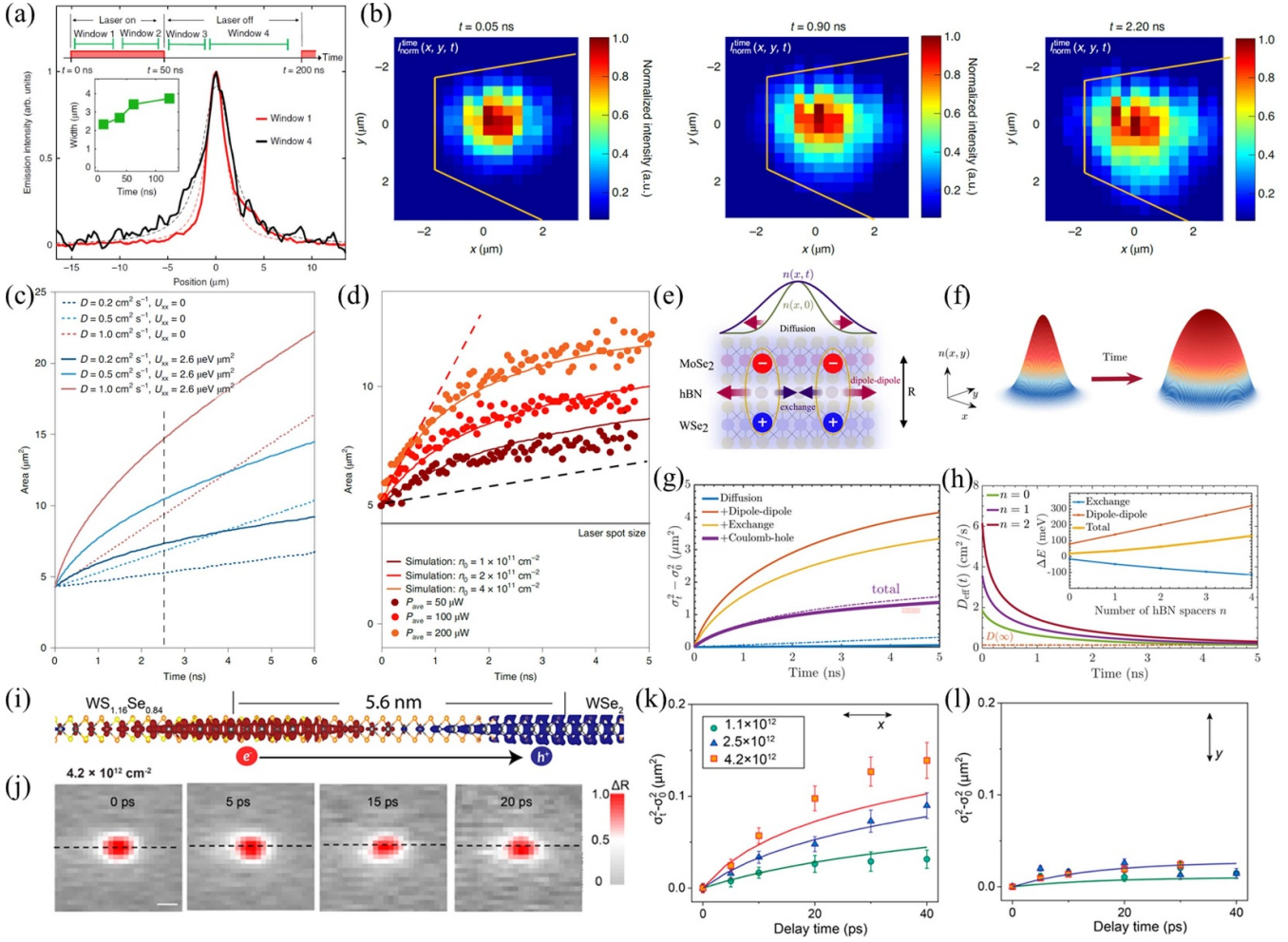
Figure 5. Transient characterization of IX diffusion and transport. (a) Spatial profiles of emission measured in different time windows excited by the laser with a pulse duration of 50 ns and a period of 200 ns in a MoS_2/3L-hBN/MoS_2 heterostructure. Reproduced from [147]. CC BY 4.0. (b) PL images of the WSe_2/hBN/$MoSe_2$ heterostructure at different times with the incident power of 200 μW. The yellow lines depict the heterostructure area. (c) Simulated exciton areas versus time for different diffusion coefficients with and without considering U_{xx}. (d) Measured exciton areas and the fitting results versus time for different excitation powers. (b)–(d) Adapted from [140], with permission from Springer Nature. (e) Schematic illustration of the repulsive dipolar interaction and attractive exchange interaction in the $MoSe_2$/nL-hBN/WSe_2 heterostructure. (f) Time evolution of spatiotemporal distribution of exciton density $n(x, y, t)$. (g) Time-dependent width of exciton distribution considering various terms. (h) Time-dependent effective diffusion coefficient for varying numbers of hBN spacers. (e)–(h) Reproduced from [164]. CC BY 4.0. (i) Local density states of the WSe_2/$WS_{1.16}Se_{0.84}$ lateral heterostructure using DFT calculation which reveals an electron-hole distance of 5.6 nm. (j) Time-dependent pump-probe transport at the lateral interface. Exciton-density–dependent $\sigma_t^2 - \sigma_0^2$ along (k) and across (l) the interface as a function of pump-probe delay times. (i)–(l) Reprinted with permission from [165]. Copyright (2023) American Chemical Society.

both repulsive (dipole–dipole) and attractive (exchange and Coulomb-hole) interactions leads to a nonlinear growth in the width of the exciton distribution. Notably, the width of the exciton distribution is reduced compared to the case where only repulsive dipolar interactions are considered. Further increasing the number of hBN spacers can enhance the repulsive dipolar interaction while reducing the exchange interaction, allowing IXs to propagate faster with larger interlayer separation (figure 5(h)).

More importantly, the utilization of transient reflection/absorption microscopy enables the imaging the spatiotemporal-dependent exciton populations, facilitating the study of ultrafast exciton diffusion on picosecond timescales. For example,

Yuan *et al* have performed time-dependent pump-probe imaging to reveal the highly anisotropic expansion of exciton cloud within 20 ps in the WSe_2/$WS_{1.16}Se_{0.84}$ lateral heterostructure, where the CT exciton population profiles along the interface exhibits a broader distribution (figures 5(i) and (j)) [165]. By fitting the mean squared displacement $\sigma_t^2 - \sigma_0^2$ using equation (3) and incorporating an extra EEA term to account for the high exciton density that enhances the exciton diffusion [162], they demonstrated that the repulsive dipolar interaction contributes to the nonlinear diffusion (figures 5(k) and (l)). This distinct exciton transport in orthogonal directions suggests anisotropic repulsive interactions, offering a potential method for reconstructing IX transport within a 1D channel.
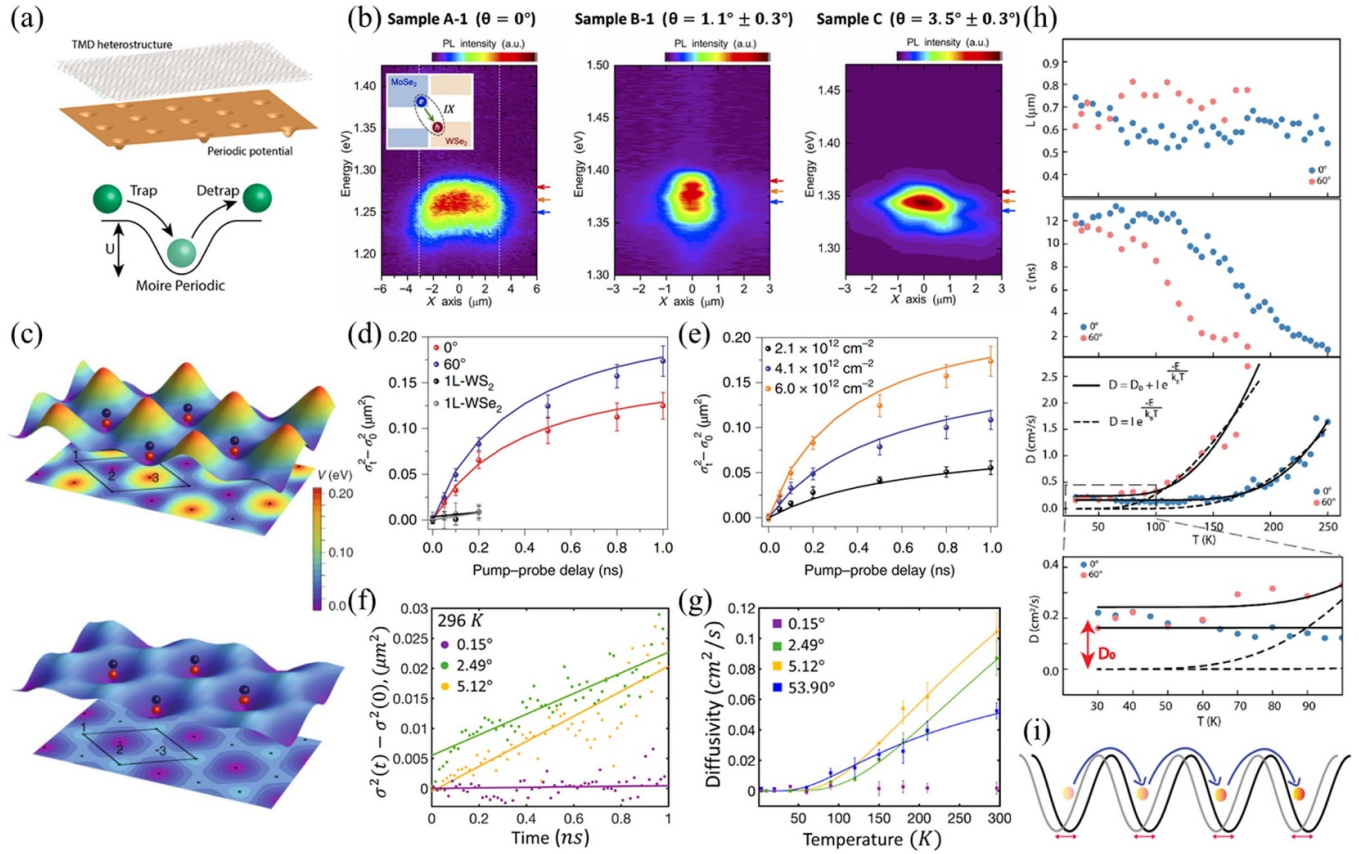
Figure 6. Moiré exciton diffusion and transport. (a) Schematic diagram of energy landscape of the TMD heterostructure and IX diffusion process within moiré potentials. Reprinted with permission from [52]. Copyright (2021) American Chemical Society. (b) Spatially resolved PL images of IXs in different WSe$_2$/MoSe$_2$ heterostructures with $\theta = 0°$, $1.1° \pm 0.3°$ and $3.5° \pm 0.3°$, respectively. From [51]. Reprinted with permission from AAAS. (c) Illustrations of the moiré potentials in 0° (top) and 60° (bottom) heterostructures. (d) Twist-angle-dependent $\sigma_t^2 - \sigma_0^2$ as a function of pump-probe delay times with the density of 6.0×10^{12} cm^{-2} in the WS$_2$/WSe$_2$ heterostructure. (e) Density–dependent IX transport of the 60° heterostructure. (c)–(e) Adapted from [149], with permission from Springer Nature. (f) Temporal evolution of $\sigma_t^2 - \sigma_0^2$ of IXs within various twisted WSe$_2$/MoSe$_2$ heterostructures. (g) Temperature-dependent diffusivity of IXs for different twist angles. (f) And (g) Reprinted with permission from [52]. Copyright (2021) American Chemical Society. (h) Temperature-dependent diffusion length, lifetime and diffusivity for 0° and 60° WS$_2$/WSe$_2$ heterostructures. (i) Schematic illustration of exciton transport assisted by moiré phasons (red arrows). (h) And (i) Reproduced from [151]. CC BY 4.0.

3.3. Moiré exciton diffusion and transport

The formation of moiré patterns introduces varying moiré potential landscapes that modify exciton emission behaviors and localize excitons [82, 83]. Nonetheless, excitons can migrate from one location to another energy minima, manifesting as trapping and de-trapping processes within moiré periodic potentials, allowing them to diffuse over long distances (figure 6(a)) [52]. However, at small twist angles, the moiré pattern exhibits deep potentials that may completely localized IXs, impeding their diffusion and transport. As depicted in figure 6(b), in the absence of moiré superlattice at zero twist angle, the spatial IX diffusion shows the longest diffusion length [51]. In contrast, when the moiré periodicity reduces from 20 nm with $\theta = 1.1°$ to 5.7 nm with $\theta = 3.5°$, IXs can tunnel between different supercells, resulting observable diffusion beyond the excitation spot size over longer lifetimes. To comprehensively describe the exciton transport in the presence of moiré potential, Knorr *et al* have developed a microscopic

approach that demonstrates the transition from the hopping regime to the dispersive regime depending on the twist angle [169]. Their model reveals that for twist angle smaller 2°, IXs are strongly localized within the moiré potential landscape, while at large twist angles, IXs transport like free particles with a modified mass. The transition between these two states provides new insights into the fundamental nature of exciton diffusion and transport in moiré superlattices and highlights the crucial importance of the twist angle in determining the exciton propagation.

In addition to the rotational misalignment that create moiré potentials to modulate exciton propagation, lattice mismatch also introduces periodic energy landscapes for the manipulation of exciton transport. Using the first principles calculation with density functional theory (DFT), Yuan *et al* have calculated the energy landscape of the moiré patterns for both 0° and 60° heterostructures with approximately 4% lattice mismatch, corresponding to a moiré periodicity of 7.6 nm [149]. Notably, the 0° heterostructure possesses a much deeper potential of

159 meV, in contrast to the 60° heterostructure which shows a shallower potential of 124 meV (figure 6(c)). Therefore, IXs exhibit reduced mobility in the 0° heterostructure, showing suppressed diffusion compared to the 60° heterostructure (figure 6(d)). Meanwhile, the acceleration of IXs at higher densities, accompanied by nonlinear temporal dependence, again confirms the presence of repulsive dipolar interactions as previously discussed [44, 105, 140, 164] (figure 6(e)).

Moreover, IXs are reported to exhibit anomalous diffusive transport when subjected to different moiré potential depths at elevated temperatures due to the non-equilibrium many-body effects [52]. This transport shows a temperature-activated diffusivity dependence on the twist angle, suggesting that thermal energy can cause the de-trapping of IXs when exceeding the moiré potential depth, except for the extremely deep potential depth of the twist angle of 0.15°, which always trap IXs even at room temperature (figures 6(f) and (g)). Besides, a recent study has compared the temperature-dependent diffusion dynamics for direct excitons in WSe_2 monolayers and indirect excitons in WSe_2 homobilayers [150]. This study demonstrated that the effective diffusivity of direct excitons initially increases from 80 K to 280 K and then decreases, whereas it remains unchanged in the 80–400 K for indirect excitons in homobilayers. This discrepancy can be attributed to the smaller disorder potentials ($\approx$17 meV) in monolayers and much larger moiré potentials ($>$50 meV) compared to the thermal fluctuation energy in homobilayers. These observations reveal the complex interplay between periodic moiré potential landscapes and the thermal energy of IXs, which can substantially alter exciton transport dynamics.

Intriguingly, unlike the previously observed temperature-dependent IX diffusion in moiré heterostructures, Rossi *et al* have unveiled an unprecedented IX diffusion mechanism assisted by the moiré-induced phonons, usually referred to as phasons [151]. While IX diffusion typically displays an Arrhenius-like behavior with temperature variation, this pioneering study demonstrates a nonzero, constant diffusivity D_0 below 90 K, indicating IXs remain mobile at relatively low temperatures for both 0° and 60° heterostructures (figure 6(h)). These observations deviate from the classical temperature-activated hopping out of the moiré potentials. Instead, by employing the classical molecular dynamics simulations, they found that moiré potentials exhibit a dynamic in-plane motion mediated by the thermally activated phasons, thereby allowing for the diffusing excitons (figure 6(i)). These simulations also reveal an increasing speed of phasons with rising temperature, reaching approximately 20 m s^{-1}. These phenomena shed light on the intricate interplay between excitons and phonons within moiré superlattice, establishing a compelling framework for the integration of phason dynamics and moiré exciton transport.

In this section, we have reviewed the diffusion dynamics of IXs and moiré excitons, with a focus on their spatial and temporal behaviors. The long-lived nature of IXs enables them travel across the heterostructure under local excitation, which can be described by the classical 2D drift-diffusion model. Numerous studies have highlighted the pronounced

exciton expansion with increasing excitation power over time, exhibiting varying dependence indicate of IX diffusion driven by different reasons, including concentration gradients, EEA, repulsive dipolar and attractive interactions. Further introduction of moiré potentials plays a critical role in governing exciton transport. Although localized moiré excitons are expected to exhibit shorter diffusion lengths in twisted heterostructures than those in untwisted heterostructures, the IX propagation can be efficiently manipulated within moiré superlattices by modulating the depth and shift of moiré potentials through variations in twist angle, or by tuning exciton density and temperature. The precise control over periodic potential landscapes, combined with the versatile diffusion dynamics of TMDs, provide a comprehensive understanding of exciton transport in TMD heterostructures, paving the way for the realization and optimization of advanced optoelectronic devices with novel functionalities.

4. Manipulation of IXs diffusion and transport

4.1. Excitonic phase transitions

Moiré superlattices, characterized by their strong light-matter interaction and flat energy bands, can host novel quantum many-body states and constitute a platform to engineer strong electronic correlations, such as correlated insulating states [170–173], Mott insulators [174–179], Bose-Einstein condensation [180–182], superconductors [183–185], charge density waves [186, 187], and Wigner crystals [188–190]. In most systems, the appearance of these correlated states can be controlled by varying the filling factors of the moiré supercell via electrostatic gating or electric fields, enabling the gate-tunable phase transitions [170–179, 182, 186, 188–191]. In addition, optical excitation density above the Mott threshold (3×10^{12} cm^{-2}) provide an alternative pathway to drive phase transition from IXs to charge-separated electron/hole plasmas [192]. Therefore, this optical carrier density control over phase transitions consequently allows for the modulation of exciton diffusion and transport properties by tuning the photoexcited carrier densities. As depicted in figure 7(a), Brem and Malic proposed that intermediate exciton densities (10^{11}–10^{12} cm^{-2}) can introduce strong dipolar repulsion between IXs that reduce effective moiré potentials and modify the exciton wave function, promoting the delocalization of moiré-trapped IXs and manipulation of density–dependent IX transport [193]. Further increasing the density beyond Mott transition, Wang *et al* have observed two distinct phase transitions for IX diffusion [152]. They demonstrated the first phase transition from moiré exciton trapping to free exciton gas as density reach 1–5 $\times$ 10^{11} cm^{-2}, accompanied by the merging of sharp moiré exciton PL peak into broaden peaks, indicating excitons escape from moiré traps (figures 7(b) and (c)). Further increasing the density beyond 10^{12} cm^{-2} above the Mott transition can enable the second phase transition from free exciton gas ionized into highly mobile electron-hole plasmas, which give rise to asymmetric spatial distribution of PL
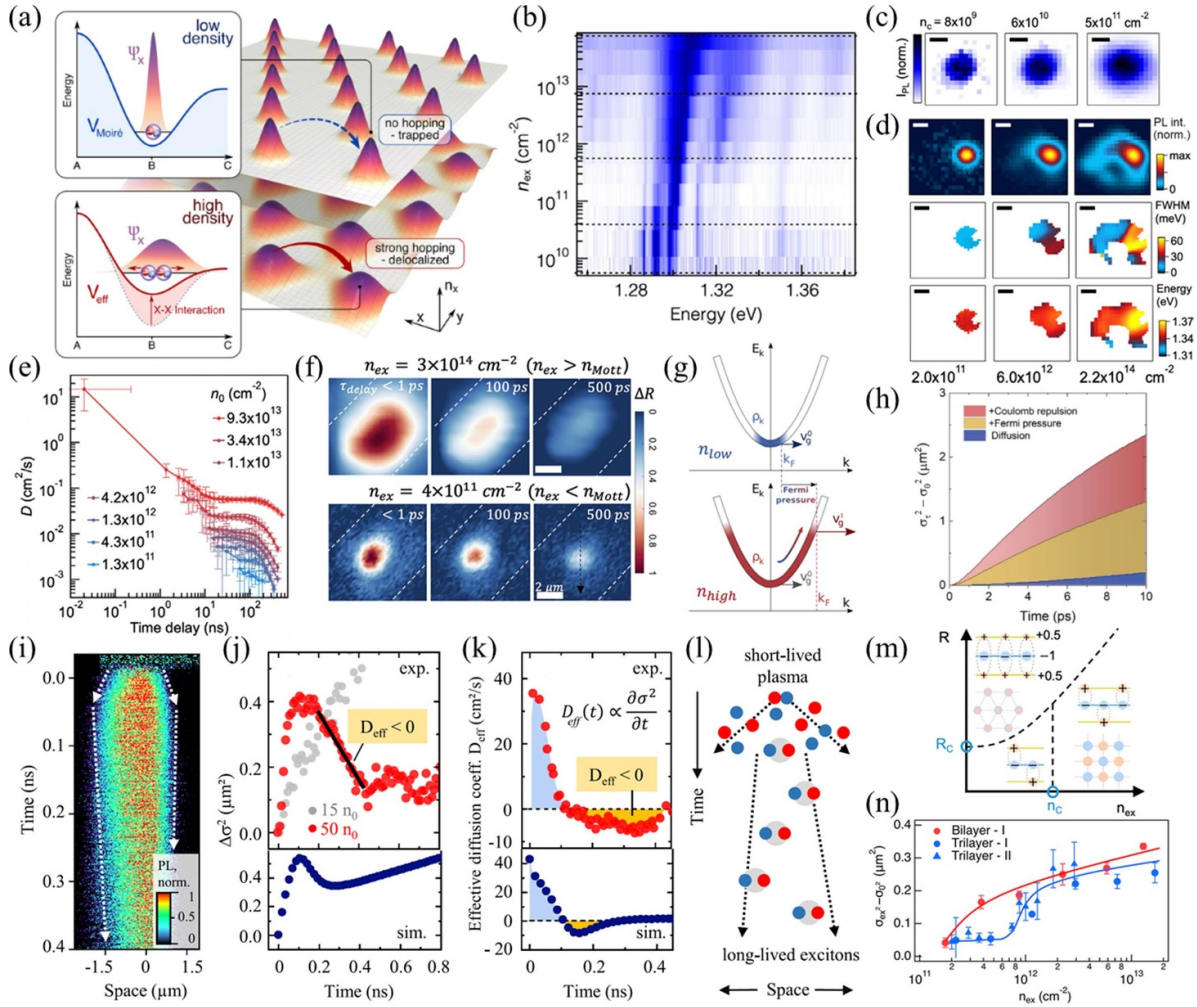
Figure 7. Density–dependent phase transition for controllable IX diffusion. (a) Schematic diagram of moiré potentials localizing excitons at low density and delocalizing excitons by reducing potential energy at high density. Reprinted with permission from [193]. Copyright (2023) American Chemical Society. (b) PL evolution of the MoSe$_2$/WSe$_2$ heterostructure as a function of density. (c) PL images of IXs at different excitation densities of 8×10^9 cm^{-2}, 6×10^{10} cm^{-2} and 5×10^{11} cm^{-2}. Scale bar, 1 μm. (d) Color plot of PL intensity, FWHM and average energy at different high excitation densities from 2.0×10^{11} cm^{-2}–2.2×10^{14} cm^{-2}. Scale bar, 2 μm. (e) Time-dependent effective diffusion coefficient at different density. (b)–(e) Reprinted figure with permission from [152], Copyright (2021) by the American Physical Society. (f) Normalized transient differential reflection images of the MoSe$_2$/WSe$_2$ heterostructure at varying delay times for low (4×10^{11} cm^{-2}) and high (3×10^{14} cm^{-2}) densities. Scale bar, 2 μm. (g) Schematic diagram of the effect of Fermi pressure on exciton transport. (h) Impact of pure diffusion, Fermi pressure and Coulomb repulsion on hot plasma expansion for the high density of 10^{14} cm^{-2}. (f)–(h) Reprinted with permission from [194]. Copyright (2023) American Chemical Society. (i) Time-resolved PL images of the MoSe$_2$/WSe$_2$ heterostructure for the density of 6×10^{12} cm^{-2}. (k) Time-resolved mean squared displacement at high (50n$_0$) and intermediate (15n$_0$) densities and the simulation results at high density. (k) Time-dependent effective diffusion coefficients at high density. (l) Schematic diagram of the two-component model for the temporal IX transport from short-lived plasma to longer-lived excitons. (i)–(l) Reprinted figure with permission from [153], Copyright (2024) by the American Physical Society. (m) Schematic illustration of phase transition with increasing density in the WSe$_2$/MoSe$_2$/WSe$_2$ trilayer. (n) Mean squared displacement as a function of excitation density for WSe$_2$/MoSe$_2$ bilayer and WSe$_2$/MoSe$_2$/WSe$_2$ trilayer. (m) And (n) Reprinted with permission from [195]. Copyright (2023) American Chemical Society.

intensity, full width at half maximum (FWHM), and average energy (figure 7(d)). Consequently, the diffusion coefficient, defined as $d\sigma^2(t)/dt$, differs with density at varying delay times. As depicted in figure 7(e), while diffusivity usually exhibits a decreasing trend with increasing delay times, the temporal diffusion coefficient at high density undergoes an initial decrease to a plateau followed by a further decrease,

revealing a two-step transition for densities exceeding the Mott threshold.

Remarkably, when the excitation density significantly surpasses the Mott density, Choi *et al* have demonstrated that this hot plasma expansion occurs on an ultrafast timescale approaching the spatial resolution limit of 0.2 ps (figure 7(f)). In addition to the repulsive interaction driving IX diffusion at

the intermediate excitation density, they further revealed that both Coulomb repulsion and Fermi pressure lead to the rapid diffusion of IXs over several micrometers at high excitation density of 10^{14} cm^{-2}, as evidenced by the microscopic calculation (figures 7(g) and (h)) [194]. Besides, other factors may also govern the IX transport, potentially introducing novel behaviors. For instance, Wietek *et al* have reported the anomalous nonlinear diffusion of IXs with increasing carrier density [153]. By comparing individual simulations of EEA and repulsion, they determined that both mechanisms contribute equally to the nonlinear propagation. Similarly, increasing the excitation density beyond the Mott threshold, they observed a rapid initial expansion within the first 50 ps attributed to the plasma propagation, followed by a propagation contraction extending to hundreds of picoseconds due to the presence of long-lived excitons (figures 7(i) and (j)). This phenomenon yields an effectively negative diffusivity of IXs, suggesting a transient crossover from plasma to excitons, enabling the efficient modulation of IX transport (figures 7(k) and (l)).

Interestingly, recent studies have unveiled the emergence of quadrupolar IXs in the symmetric trilayer structures, in which electrons (holes) are confined in the middle layer and holes (electrons) reside in both top and bottom layers (figure 7(m)) [196–199]. Unlike dipolar IXs which possess permanent dipolar moments, quadrupolar IXs are the superposition of the two dipolar IXs with opposing polarities, showing two branches with opposite Stark shifts due to the layer hybridization. Consequently, quadrupolar IXs may display distinct transport behaviors compared to dipolar IXs, particularly as exciton density varies. Bai *et al* have investigated the exciton diffusion of dipolar IXs and quadrupolar IXs in the bilayer and trilayer structures, respectively, demonstrating the formation of robust exciton crystals and the occurrence of quantum phase transitions in trilayer with increasing exciton density [195]. As shown in figure 7(n), while dipolar IXs present a monotonical expansion from moiré trapped excitons to free exciton gas and eventually to electron-hole plasmas, quadrupolar IXs remain nearly immobile for densities below 5×10^{11} cm^{-2} but followed by a sharp increase in diffusion. These observations reveal the transition from quadrupolar exciton crystal to the dipolar exciton phase, further motivating the exploration of exciton transport enabled by phase transitions.

Moreover, apart from the density-induced phase transition that can manifest itself to regulate IX migration, temperature modulation can also significantly control the exciton transport behavior via phase transition. As previously discussed, moiré potentials tend to trap excitons at low temperatures, but delocalize them to free excitons once the thermal activation overcomes moiré potentials at elevated temperatures [52, 123, 150]. Therefore, the transition in IX transport from classical free exciton gas to exciton degeneracy states can be demonstrated with decreasing temperature. According to Liu *et al*, this phase transition occurs at around 30 K and shows a sudden drop in the diffusivity [200]. These manipulations offer novel and accessible approaches to control the exciton mobility,

thereby advancing the understanding the many-body states for the application of excitonic devices.

4.2. Dielectric engineering

The dielectric screening, determined by the immediate surroundings or substrates, has been reported to play an important role in controlling the exciton transport dynamics in monolayer TMDs [4, 7, 201–203]. In this situation, the Coulomb interaction can be tuned by varying the dielectric environment, which exhibit strong modulation effect on electronic bandgaps, exciton linewidths, and exciton binding energies [202, 204, 205]. Specially, the integration of hBN encapsulation effectively suppresses the dielectric disorder from the substrate for TMD monolayers, leading to intrinsic optical properties and faster exciton propagation with increased diffusion coefficients [4, 202, 203]. Similarly, the top and bottom surrounding media with larger dielectric constant exhibit a stronger dielectric screening effect, which has also been demonstrated to efficiently reduce the binding energy of IXs [206–209]. As illustrated in figure 8(a), the band gap energy E_{CT}^0 and exciton energy X_{CT} exhibit redshifts with increasing dielectric constant ε due to the reduced Coulomb interactions, leading to a considerable decrease in the exciton binding energies X_{CT}^b, ranging from nearly 200 meV in the free-standing situation ($\varepsilon = 1$) to 63 meV in the SiO$_2$-air case ($\varepsilon = 2.4$) and ultimately to just a few meV in the hBN-encapsulated environment ($\varepsilon = 4.5$). Meanwhile, the X_{CT}^b decreases with increasing exciton dipole, corresponding to the increasing interlayer spacing of IXs [209, 210]. Therefore, IXs are weakly bound in high-dielectric environments. Together with the substrate surface passivation, IXs are hence more easily to transport in vdW heterostructures.

On this basis, Erkensten *et al* have developed a microscopic theory to elucidate the interplay between IX-exciton interactions and IX transport affected by varying the surrounding dielectric environments [164]. They demonstrated that while the repulsive dipole–dipole and attractive exchange interactions are independent of dielectric screening, the Coulomb interaction is gradually weakened with increasing dielectric constant (figure 8(b)). Therefore, the strong dielectric screening can introduce a pronounced Coulomb drift, enabling the acceleration of IX propagation in the hBN-encapsulated heterostructures compared with the freestanding cases or those deposited on SiO$_2$ substrates (figure 8(c)).

On the other hand, the reduced binding energy of IXs surrounded by high-dielectric environments will in turn hinder the formation of IXs [96]. In contrast, the suspended heterostructure without dielectric screening hold potential for higher formation efficiency of IXs, contributing to highly enhanced IX emission intensities (figures 8(d) and (e)) [154]. Thus, the intrinsic IX transport properties can be fully studied in the freestanding heterostructure. As shown in figure 8(f), IXs are completely localized by the moiré potential at density below 1.49×10^{11} cm^{-2}, but strikingly mobile for a larger density of 1.15×10^{12} cm^{-2} (<Mott density) due to the strong IX
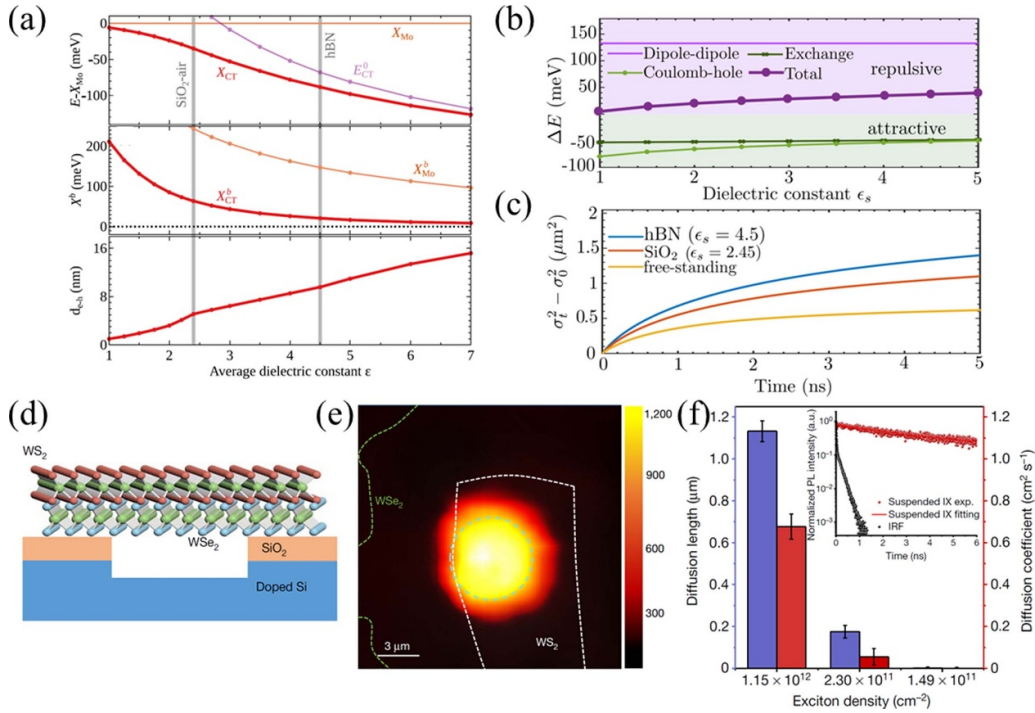
Figure 8. Dielectric engineering of exciton characteristics and diffusion. (a) CT exciton energy, binding energy and exciton dipole as a function of dielectric constant in the lateral MoSe$_2$/WSe$_2$ heterostructure. Reproduced from [207]. CC BY 4.0. (b) Energy renormalization contributed by different interaction terms as a function of dielectric constant in the MoSe$_2$/WSe$_2$ heterostructure. (c) Time-dependent $\sigma_t^2 - \sigma_0^2$ for various dielectric environments. (b) And (c) Reproduced from [164]. CC BY 4.0. Schematic diagram (d) and PL mapping (e) of the suspended WS$_2$/WSe$_2$ heterostructure. Scale bar, 3 μm. (f) Diffusion length and diffusion coefficient for various exciton densities. The inset shows time-resolved PL spectra of IXs exhibiting a lifetime of 9.5 ns. (d)–(f) Adapted from [154], with permission from Springer Nature.

pair correlation influenced by the dipole–dipole interactions. In contrast, a very recent study found the enhanced emission from more localized moiré excitons only at the edge of this circular hole due to the deeper moiré potential induced by the uniaxial strain [211], which may give rise intriguing diffusion behaviors. Therefore, the combination of different factors should take into consideration when studying IX diffusion.

Overall, the dielectric engineering provides a promising stage to manipulate the exciton optical properties and transport dynamics. The dielectric screening can efficiently amplify the dipolar interactions and modify the emergence of correlated IX phases [212, 213]. Besides, the dielectric screening effect can reduce the carrier and phonon scattering, resulting in prolonged energy relaxation, further recasting the exciton diffusion [214]. These phenomena strengthen the feasibility of controlling exciton transport via dielectric engineering, which can unlock new avenues for exploring exciton behaviors in emerging excitonic and optoelectronic devices.

4.3. Electric control

IXs possess permanent out-of-plane dipole moment $\boldsymbol{p}$ which can be tuned by vertical external electric field $\boldsymbol{E}$, thus the resulting energy landscape monitored by the linear Stark effect $\Delta\varepsilon = -\boldsymbol{p} \cdot \boldsymbol{E}$ significantly guides the IX movement. To reinforce this electrically controllable exciton transport, the insertion of an atomic monolayer hBN between two layers

can strengthen the dipole moment while simultaneously reducing the moiré potential (figure 9(a) [90]. The slope of energy shift give rise to a larger dipole size of 0.9 nm compared with 0.6 nm in the structure without the hBN separator, allows for stronger modulation of IX transport (figure 9(b)). By tailoring the electric field, IXs tend to flow towards the lower energy sides, diffuse freely in flat potentials, or be confined by higher energy barriers near the gate edges. Similar phenomena can also be observed for valley-polarized IXs. In particular, focusing on the exciton diffusion upon exposure in the splitting gate region, IXs exhibit three typical diffusion regimes: anti-confinement (potential barrier), free diffusion (zero potential) and confinement (potential trap) (figures 9(c)–(d)). While the anti-confinement regime promotes IXs dispersal away from the excitation point, resulting in a two-lobe exciton cloud, the confinement regime significantly constrains IXs in the gate region with strong exciton–exciton interactions. Consequently, the energy shift exhibits a nonlinear relationship, which can be described by $\Delta\varepsilon = -\boldsymbol{p} \cdot \boldsymbol{E} + n_{IX}de^2/\varepsilon_{HS}\varepsilon_0$. This suggests that the confining electrostatic potential can effectively trap IXs to increase their densities, as reported in a very recent study that demonstrated an IX ionization transition in a tunable electrostatic trap, representing a significant advancement towards exciton condensates [163].

Furthermore, by recording the spatially and temporally resolved PL images of IX cloud, Sun *et al* have revealed the
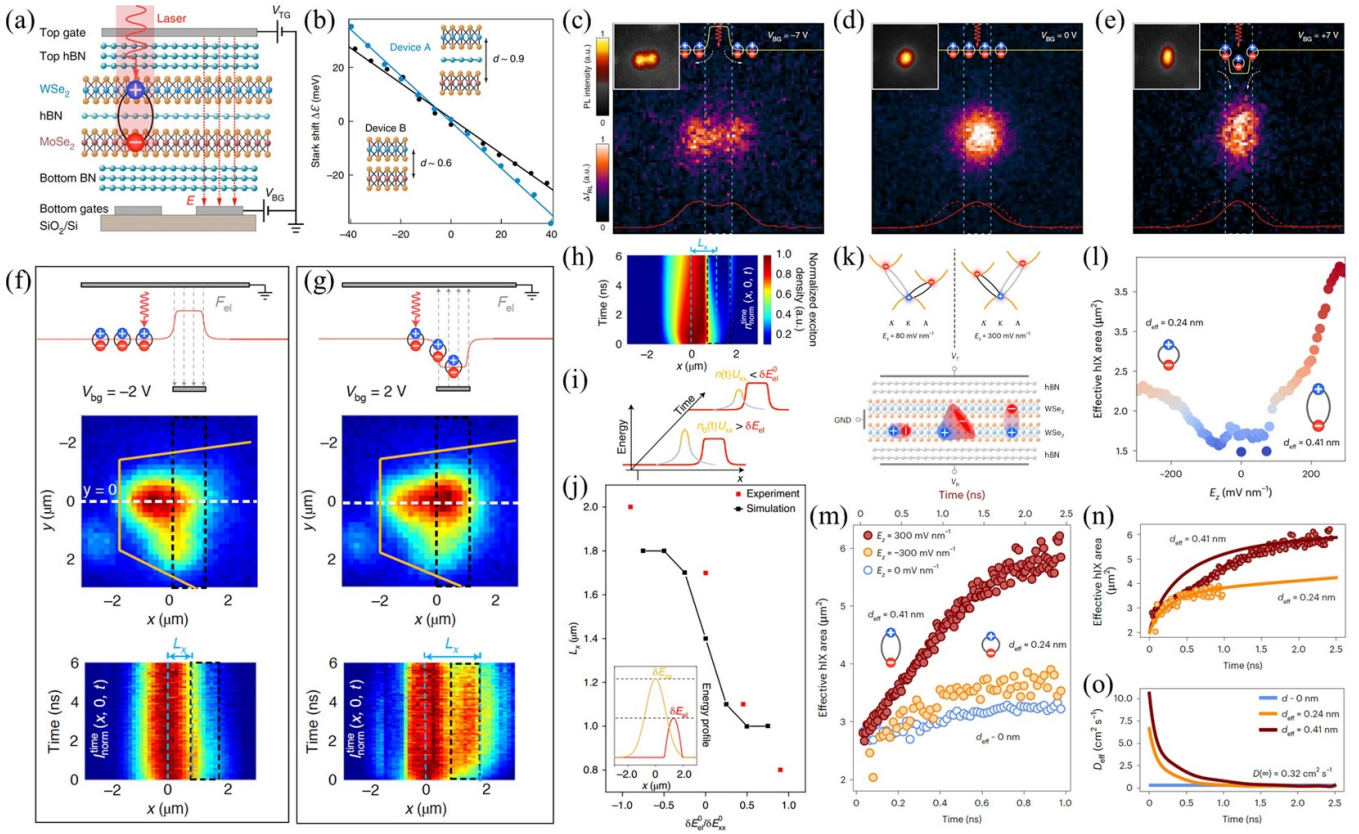
Figure 9. Electric control of IX transport. (a) Schematic diagram of the WSe$_2$/hBN/MoSe$_2$ heterotrilayer. (b) Energy shift of IXs as a function of vertical electric field in two types of devices. CCD images of IX cloud polarization for exciton dynamic regimes of anti-confinement (c), free diffusion (d) and confinement (e). Insets show the corresponding PL intensity images. (a)–(e) Adapted from [90], with permission from Springer Nature. Schematic diagram of exciton energy profiles, CCD images of PL intensity and time-dependent PL intensity of IXs for the barrier (f) and trap (g) cases. (h) Simulation of the temporal exciton distribution for the ratio around 0.5. (i) Schematic diagram of the temporal evolution of energy profile of $\delta E_{\rm el}$ and $E_{\rm XX}(t)$. (j) Exciton propagation distance as a function of $\delta E_{\rm el}^0/E_{\rm XX}^0$. The inset shows the simulated energy profiles. (f)–(j) Adapted from [140], with permission from Springer Nature. (k) Schematic diagram of the band structure under different electric field strengths and the homobilayer WSe$_2$ device. (l) Steady-state effective hybrid IX diffusion area with respect to electric field. Time evolution of measured (m) and stimulated (n) effective hybrid IX areas at different electric fields. (o) Effective diffusivity extracted from the theoretical simulation. (k)–(o) Reproduced from [155]. CC BY 4.0.

dynamic interplay between electric fields and exciton–exciton interactions in shaping IX transport using the same device structure [140]. While the time-independent electrostatic potential $\delta E_{\rm el}$ varied by external electric fields can effectively control the IX motion, the energy profile of repulsive dipolar exciton–exciton interactions $\delta E_{\rm XX}$ also imposes a drift term in the exciton diffusion model (equation (3)). As shown in figures 9(f) and (g), by tuning the gate voltage, IXs can be effectively blocked by potential barriers or directed towards potential traps, resulting in distinct migration dynamics in both time and space. In the barrier case, IXs remain restricted without time dependence before reaching the gate region. Conversely, in the trap case, IXs initially move towards the potential trap within 1 ns, followed by an intriguing shrink back (figure 9(h)). This anomalous exciton transport arises from the temporally comparable competition between $\delta E_{\rm el}$ and $\delta E_{\rm XX}$, where $\delta E_{\rm XX}$ dominates at short timescales, enabling IXs to flow towards the gate region, and then $\delta E_{\rm el}$ becomes prominent away from the gate region due to the reduced spatial density (figure 9(i)). This dynamic interplay allows for electrically

precise control of IX transport by varying the ratio of $\delta E_{\rm el}$ to $\delta E_{\rm XX}$, paving the way for manipulating IX propagation over specific distances (figure 9(j)).

Beyond tuning IX transport through the construction of electrically reconfigurable energy barriers or traps, the layer hybridization of exciton states, comprising intralayer and interlayer components, can also be modulated by the vertical electric field, giving rise to controllable hybrid IX transport [155, 215]. As illustrated in figure 9(k), Tagarelli *et al* have reported a shift in the lowest transition from KΛ to KΛ′ in the WSe$_2$ homobilayer with increasing interlayer mixing in the layer hybridization at elevated electric fields. The observed asymmetric field-dependent energy shift, owing to the intrinsic doping of the natural WSe$_2$, yields dipolar ensemble length of 0.24 nm and 0.41 nm at high positive and negative electric fields, corresponding to lower and greater interlayer mixing, respectively [89]. Consequently, by tuning the hybridization and dipole length, layer-hybridized IXs exhibit variable exciton cloud due to the interplay between repulsive dipolar interactions and attractive exchange interactions (figure 9(l)).

The spatiotemporal imaging of exciton distribution revealed an anomalous diffusion for hybrid IXs under both high positive and negative electric fields, contrasting with the linear expansion observed at negligible fields (figure 9(m)). In addition, while hybrid IXs demonstrated an intrinsic diffusivity of 0.32 cm^2 s^{-1}, the stimulation of time-dependent exciton diffusion estimates an initially effective diffusivity of 7 cm^2 s^{-1} and 11 cm^2 s^{-1} for low-d (0.24 nm) and high-d (0.41 nm) dominated ensembles, respectively (figures 9(n) and (o)). This spatial manipulation underscores the highly tunable layer-hybridized IX diffusion, characterized by different effective dipole lengths with electric control. Besides, further modulating the exciton states from charged IXs to charged intralayer exciton emission by electrical switching from type-II to type-I band alignment, the diffusion length exhibits a tunable range of 1.99–2.89 μm in the WS$_2$/(iso-BA)$_2$PbI$_4$ heterostructure [216]. These phenomena highlight the feasibility of electrically controllable exciton diffusion by regulating the dipole sizes or the exciton states, a step towards realizing exciton condensates by the manipulation of many-body effects.

Moreover, electric fields also provide a powerful stage to control the diffusion of moiré excitons. According to the first-principle calculation on moiré excitons, Guo *et al* have predicted that electric fields can significantly influence the degree of exciton hybridization [108]. This suggests that alternating electric fields can induce oscillating dipoles of moiré exciton to modulate the exciton diffusion. Besides, since the moiré potential can be tuned by electric fields [106, 135], Fowler-Gerace *et al* have realized long-range IX propagation control, achieving a maximum 1/e decay distance over 13 μm in a moiré superlattice [156]. This electrical tunability arises from the reduced moiré potential with increasing electric field, in contrast to the known mechanism of electric-field-induced energy landscape variations as previously discussed. Further employing etched gates to generate spatially varying electric field, it is possible to engineer the moiré potential promote exciton condensates [180].

Therefore, with gate-tunable exciton oscillator strength [217], IXs exhibit efficient electrical control over spatial diffusion and transport through various mechanisms. In addition to the tunable exciton diffusion of these neutral IXs in the presence of out-of-plane electric fields, the motion of charged IXs can also be controlled by applying in-plane electric fields. This results in charged IXs drift towards the heterostructure boundary under the drain-source bias, allowing for controllable IX currents by changing the doping polarity of IXs or reversing the bias direction [44]. These diverse approaches demonstrate the feasibility and versatility of electrically controllable IX flux, opening new avenues for achieving excitonic devices in dilute regimes based on vdW heterostructures.

4.4. Other modulation strategies

Base on the efficient electrical tunability of IX transport, the incorporation of surface acoustic waves (SAW) can further amplify the effect of electrical regulation, leading to a significantly extended tunable diffusion range. For instance, the employment of piezoelectric substrates (e.g. LiNbO$_3$) can generate SAW to manipulate the exciton transport at elevated temperatures [157, 218]. The propagating SAW creates a time-varying piezoelectric field with dynamic potential traps that move in tandem with SAW, allowing IXs to localize in the energy minimum and travel along with the propagating SAW over long distance, akin to surfing on a wave (figure 10(a)). As a result, when the SAW is turned off, IXs diffuse freely with a limited diffusion length of 1–2 μm (figure 10(b)). Conversely, with the SAW activated, IXs travel in the direction of SAW propagation, resulting a diffusion length of ∼20 μm, constrained by the device size (figure 10(c)). This spatial modulation of propagating exciton potential facilitates a long-range directional SAW-driven IX transport, suggesting that SAW serves as an effective, contact-free method to control the IX propagation.

In addition, a recent study has involved the deposition of the TMD heterostructure onto a patterned gold substrate, aiming to generate near-field coupling of IXs to surface plasmon polaritons (SPPs) (figure 10(d)). This configuration allows for the long-distance IX migration over tens of micrometers [158]. As depicted in figure 10(e), emission beyond the excitation spot appears in both up slit and down slits across the entire 46 μm-long device. This phenomenon cannot be solely explained by the pure diffusion of IXs, as the free diffusion length typically spans only a few micrometers. In this context, Wang *et al* proposed that photogenerated excitons couple with the gold strip through near-field coupling, forming SPPs that propagate along the strip and emit from the heterostructure and monolayer TMD regions. Notably, the PL emission at both slits consists of the in-plane intralayer excitons from both TMD monolayers and out-of-plane IXs from the heterostructure, suggesting the efficient coupling of in-plane and out-of-plane optical dipoles to SPPs (figure 10(f)). More importantly, the valley polarization of IXs has also been successfully transferred to SPPs, maintaining polarization for both singlet and triplet IXs over the propagation distances of approximately 10–20 μm. Such observation is unprecedented since the intralayer excitons usually exhibit limited diffusion distances due to their relatively short lifetimes [3, 8, 9]. Therefore, its's of great importance to incorporate customized structures into vdW heterostructures, significantly enhancing IX transport and further benefitting the innovative development of advanced optoelectronic applications.

In this section, we have reviewed the effective control of IX transport over long distance. Firstly, the density–dependent excitonic phase transition can introduce substantial variation in exciton transport. Specially, tuning the excitation density allows for transitions among moiré trapped excitons, free exciton gas, and electron-hole plasms. These states exhibit distinct density–dependent diffusivities with varying time delays, and can be further tuned by temperatures. Secondly, by modifying the surrounding dielectric constant, IXs can be engineered for different propagation behaviors. They either propagate rapidly due to weak dielectric disorder and enhanced Coulomb drift in high-dielectric surroundings (e.g. hBN encapsulation), or facilitate their formation with
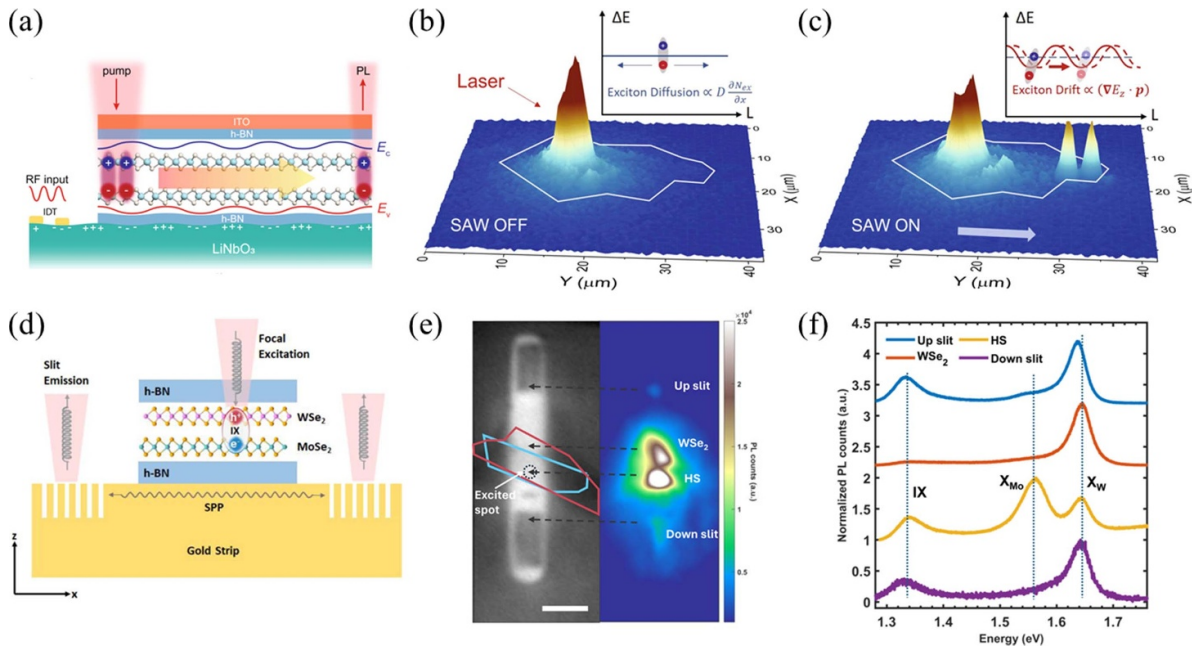
Figure 10. Customized structure incorporation to manipulate the IX transport. (a) Schematic illustration of bilayer WSe$_2$ stacked on SAW device. 3D plots of real-space PL images when the SAW is off (b) and on (c). The white lines outline the heterostructures. Insets show the free diffusion and SAW-driven transport of IXs. (a)–(c) Reproduced from [157]. CC BY 4.0. (d) Schematic illustration of the MoSe$_2$/WSe$_2$ device placed on slit-etched gold strip. (e) Optical image and PL images of the SPP device. Scale bar, 10 μm. (f) Normalized PL spectra from four regions of the device. (d)–(f) Reprinted from [158], with the permission of AIP Publishing.

reduced dielectric screening (e.g. freestanding case) to investigate the correlated IX diffusion in low-dielectric environments. Thirdly, the electrical control of IXs leads to dynamic spatiotemporal diffusion and transport. This control can be efficiently achieved by modulating the energy landscape, the extent of layer hybridization or the fluctuant moiré exciton and potential, enabling precise manipulation of IX diffusion and transport pathways. Finally, the incorporation of special designed structures can introduce novel phenomena, offering intriguing mechanisms to manipulate exciton flux. The piezoelectric substrate can generate kinetic electric fields that guide IXs transport along the SAW, while the gold substrate facilitates efficient coupling of both interlayer and intralayer excitons to SPPs, enabling long-distance propagation over tens of micrometers. These compelling strategies of excitonic manipulation offer a rich platform for controlling IX transport in vdW heterostructures, unlocking new possibilities for regulating light-matter interactions and advancing novel quantum technologies.

5. Applications

5.1. Excitonic devices

Since the long-lived IXs allows for long-range transport that can be further controlled by electric field via introducing energy potential barriers or wells by linear Stark effect, IX propagation can be electrically confined and spread to serve as compelling platforms for electrically operated excitonic devices and circuits [45, 47, 57]. These devices interconnect electronic and photonic signal processing, enabling photons transform into excitons which diffuse along the sample and final convert into light emission. The exciton flux can be efficiently controlled from the input to output ports and have been demonstrated as all-optical excitonic transistors in coupled quantum wells [219–221]. However, due to the rather small binding energy of approximately 10 meV, the pioneer excitonic transistors usually require very low operating temperatures, limiting the practical applications of IXs. Leveraging that IX's binding energy larger than thermal energy ($k_B T \approx 25$ meV) and nanosecond lifetimes in TMD heterostructures, Unuchek *et al* have reported the first room-temperature excitonic transistor made of MoS$_2$/WSe$_2$ heterostructures [159]. As illustrated in figure 11(a), three narrow graphene electrodes are implemented to induce gate voltages (V_{g1}, V_{g2}, V_{g3}) to engineer potential landscapes and thus control the IX flux along the channel. Under $V_{g1} = V_{g2} = V_{g3} = 0$, IXs diffuse freely inside the heterostructure over a distance of 3–5.5 μm and emit out on the edge, corresponding to the ON state of the excitonic transistor. In contrast, by setting $V_{g1} > 8$ V to introduce a potential barrier higher than $k_B T$, IX diffusion is highly terminated and thus resulting in an OFF state (figures 11(b) and (c)). Such phenomena enable the manipulation of exciton transport over several micrometers and the excitonic transistor with an ON/OFF ration exceeding 100, highlighting the potential of IXs as a foundation for high-performance, next-generation excitonic devices. Later on, they further demonstrated a valley-polarized excitonic transistor, where the valley-contrasting IXs can
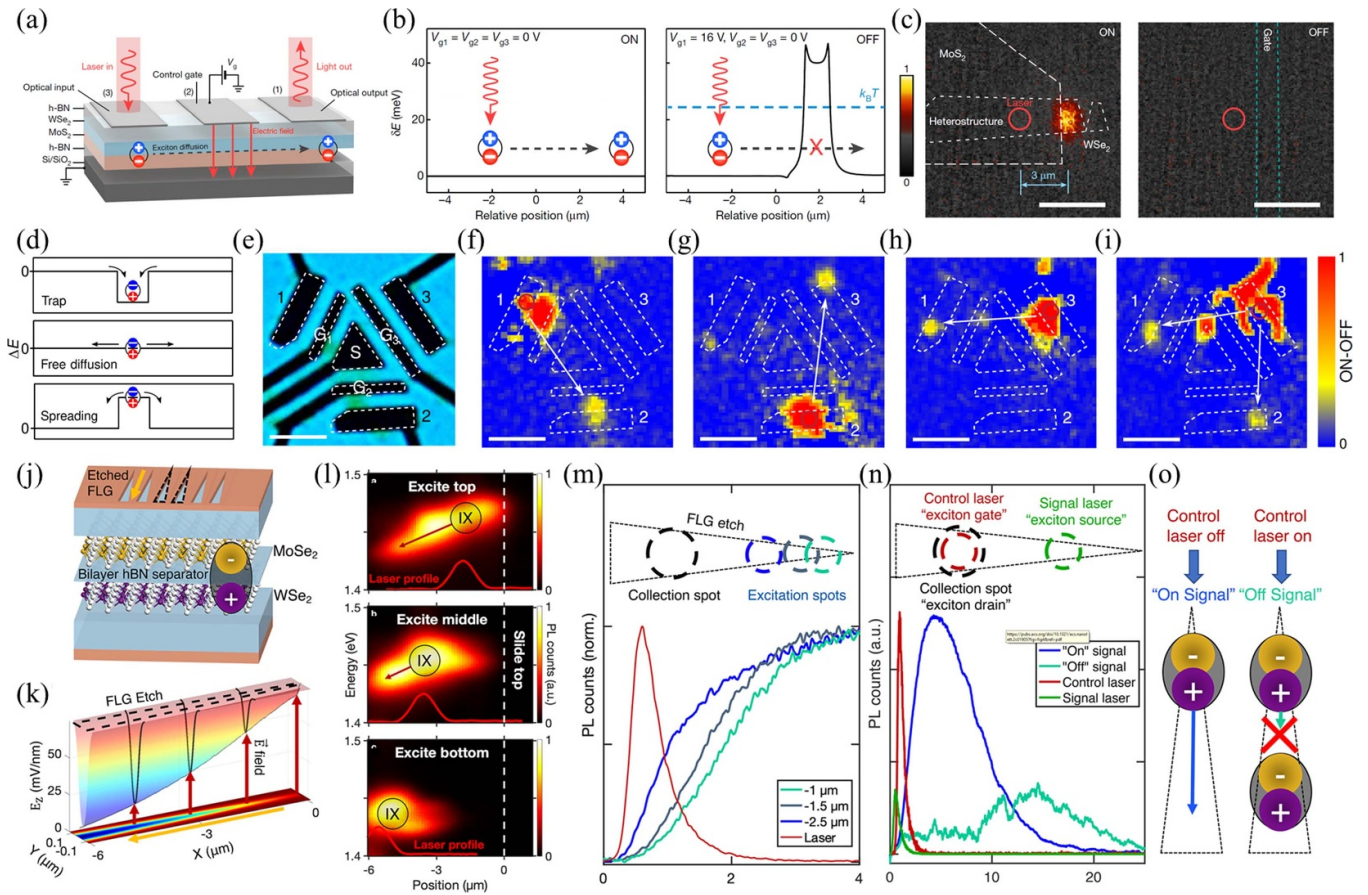
Figure 11. Excitonic devices. (a) Schematic diagram of the MoS_2/WSe_2 excitonic transistor. (b) Calculated energy variation under different gate voltages, illustrating the ON (free diffusion) and OFF (potential barrier) states. (c) Corresponding CCD images of the excitonic transistor. Scale bars, 5 μm. (a)–(c) Adapted from [159], with permission from Springer Nature. (d) Schematic diagram of energy landscapes for exciton dynamic regimes of trap, free diffusion and spreading. (e) Optical image of the excitonic router based on bilayer WSe_2. (f) Exciton propagation from port 1 to port 2 when $V_1 = 0$ V, $V_3 = 3$ V, $V_{2,ON} = -3$ V, and $V_{2,OFF} = 3$ V. (g) Exciton propagation from port 2 to port 3 when $V_1 = 8$ V, $V_2 = 0$ V, $V_{3,ON} = -1$ V, and $V_{3,OFF} = 10$ V. (h) Exciton propagation from port 3 to port 1 when $V_2 = 4$ V, $V_3 = 0$ V, $V_{1,ON} = -0.5$ V, and $V_{1,OFF} = 6$ V. (i) Excitons propagation from port 3 to both port 1 and port 2 when $V_3 = 0$ V, $V_{1,ON} = 0$ V, $V_{1,OFF} = 8$ V, $V_{2,ON} = 0$ V, and $V_{2,OFF} = 8$ V. Scale bars, 5 μm. (d)–(i) From [160]. Reprinted with permission from AAAS. (j) Schematic diagram of the $MoSe_2$/hBN/WSe_2 device. (k) COMSOL calculation of the varying electric field in the etched graphene region. (l) Spatial mapping of excitonic diode with excitation position near $x = -2$ μm, -4 μm and -6 μm. (m) Time-resolved PL spectra with localized bottom collection position and various excitation positions. (n) Depiction and time-resolved PL data of the optically gated excitonic transistor. (o) Schematic diagram of the IX flow controlled by the bottom IX population. (j)–(o) Reprinted with permission from [161]. Copyright (2022) American Chemical Society.

be electrically controlled and switched, leading to a valley exciton diffusion distance of $\sim$1.3 μm between the ON and OFF states [90].

Employing this electrically reconfigurable energy landscape, IXs could be driven to the lower energy region, yielding three typical motion regimes as previously discussed (figure 11(d)) [160]. Therefore, by changing the gate voltage to alter the operating regime, Liu *et al* have demonstrated excitonic routers to achieve the point-to-point IX movement. They designed an excitonic circuit consisting of three transistors with three ports (figure 11(e)). The application of different gate voltages among these three ports allows for IXs transmit either one port or two ports, enabling a highly programmable all-optical router (figures 11(f)–(i)). These findings establish flexible IX distribution and propagation with electrical control,

representing a critical step towards fully integrated, on-chip all-optical exciton-based applications.

Interestingly, recently studies have found that the lithographically nanopatterned graphene electrodes can introduce sharply varying electric field, thus creating electrostatic traps that modulate IX behavior [222, 223]. Taking advantage of this feature, Shanks *et al* have developed triangularly etched graphene to create a potential energy slide to effectively control IX flow (figures 11(j) and (k)) [161]. The strength of the electric field varies from 40 mV nm^{-1} to 95 mV nm^{-1}. Upon exposure to laser excitation, the IX current exhibits a unidirectional flow from the high electric field region to the low electric field region, making the application of excitonic diodes possible. As shown in figure 11(l), moving the excitation position from top to bottom preferentially directs excitons toward the
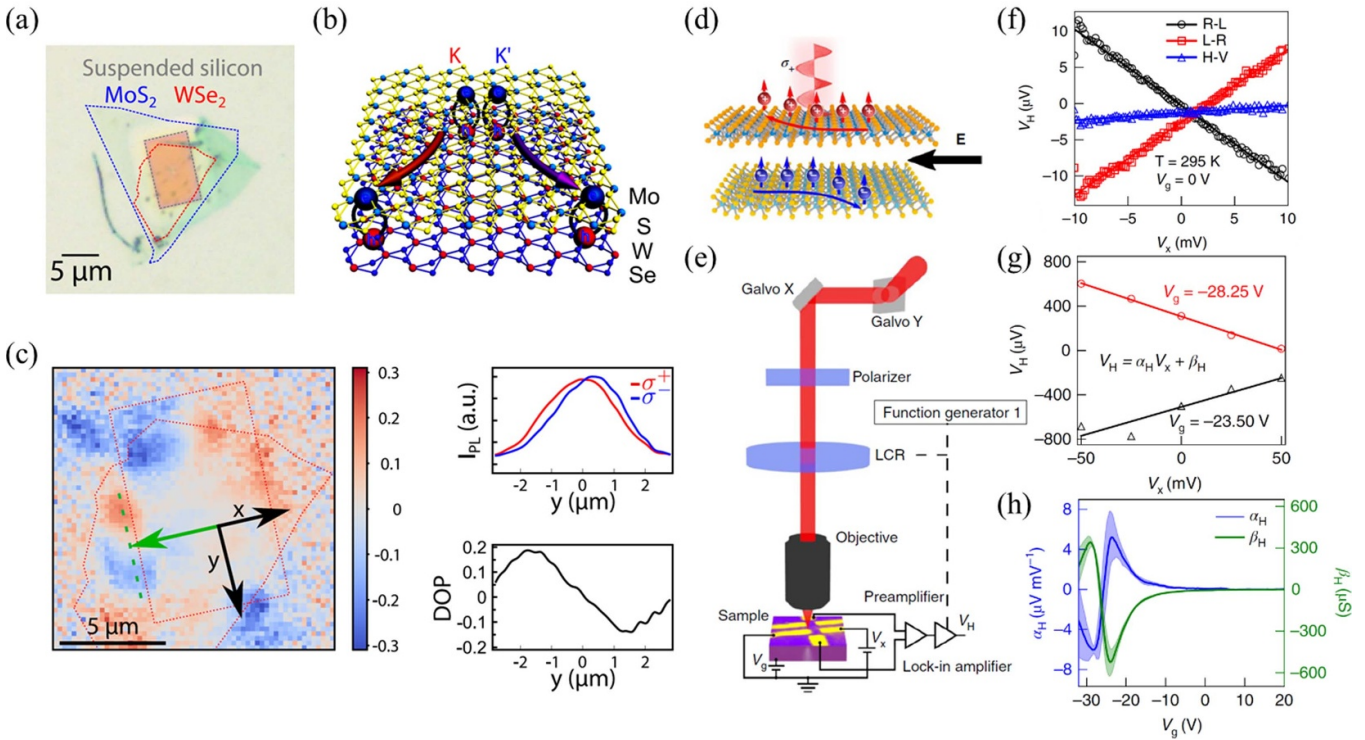
Figure 12. VHE transistors. (a) Optical image of the MoS_2/WSe_2 heterostructure on a rectangular suspended silicon-on-insulator substrate. (b) Schematic illustration of IXs in different valleys transport transversely in opposite directions under the control of Berry curvature and external strain. (c) Polarization-resolved PL mapping, cutline profiles and associated degree of polarization at room temperature. The green arrow indicates the exciton transport direction. Scale bar, 5 μm. (a)–(c) Reprinted with permission from [232]. Copyright (2020) American Chemical Society. (d) Schematic diagram of the VHE in the MoS_2/WSe_2 heterostructure. (e) Experimental setup of the VHE measurement. (f) VHE measurement under different polarization modulation. R-L stands for right- and left-circular polarization. L-R represents left- and right-circular polarization. H-V denotes horizontal and vertical polarization. (g) Hall voltage as a function of bias voltage with linear fittings at the back-gate voltage of -23.50 V and -28.25 V, respectively. (h) Gate-dependent α_H (proportional to Hall conductivity) and β_H (proportional to circular photocurrent). (d)–(h) Adapted from [233], with permission from Springer Nature.

left side, which corresponds to the lower potential energy. The spatially varying electric field caused by the sliding IX potential, combined with repulsive dipolar interactions enhanced by the confined physical channel, enable IX velocity to reach 2×10^6 cm s^{-1} (figure 11(m)). Meanwhile, the exciton density can be modulated by optical pumping with a second laser pulse, resulting in an optically gated excitonic transistor with an ON/OFF ratio of 8:1 for $t = 0$–10 ns (figures 11(n) and (o)). These novel excitonic architectures facilitate the realization of high-speed, low-loss excitonic circuit, opening new avenues for investigating the bosonic transport within low-dimensional channels

5.2. Valleytronic transistors

The VHE describes the opposite anomalous velocity of carrier transport in different valleys, manifesting as valley currents that flow in opposite directions [24]. Due to the broken inversion symmetry and preserved time-reversal symmetry in monolayer TMDs, the Berry curvature at $\pm$K points exhibit opposite signs [56, 224]. Therefore, carriers

in $\pm$K valleys experience opposite Berry curvatures, leading to transverse flow in opposite directions and accumulation at opposing edges under the in-plane electric field, giving rise to measurable Hall voltages or currents [224, 225]. The VHE has been extensively investigated in monolayer TMDs, yielding a comprehensive understanding [55, 226–228]. However, compared to the rapid valley depolarization of intralayer excitons occurring on picosecond timescales [42, 229, 230], IXs in TMD heterostructures exhibit prolonged valley lifetimes extending into the microsecond range, which is more conducive to the observation of VHE [41, 231]. This remarkable enhancement further allows for the observation of VHE in IXs under ambient conditions. Huang *et al* have achieved the room-temperature VHE of IXs for the first time in a uniquely designed device geometry [232]. They utilized suspended slab, bent by gravity on an etched substrate, to induce strain that generates strong potential gradients at the edges to achieve the observation of the VHE (figures 12(a) and (b)). Along the transport of IXs to the sample edge, IXs in $\pm$K valleys are expected to traverse towards opposite directions under linearly polarized excitation due to the presence of VHE. Therefore, the σ^+ and σ^- components of IX emission become
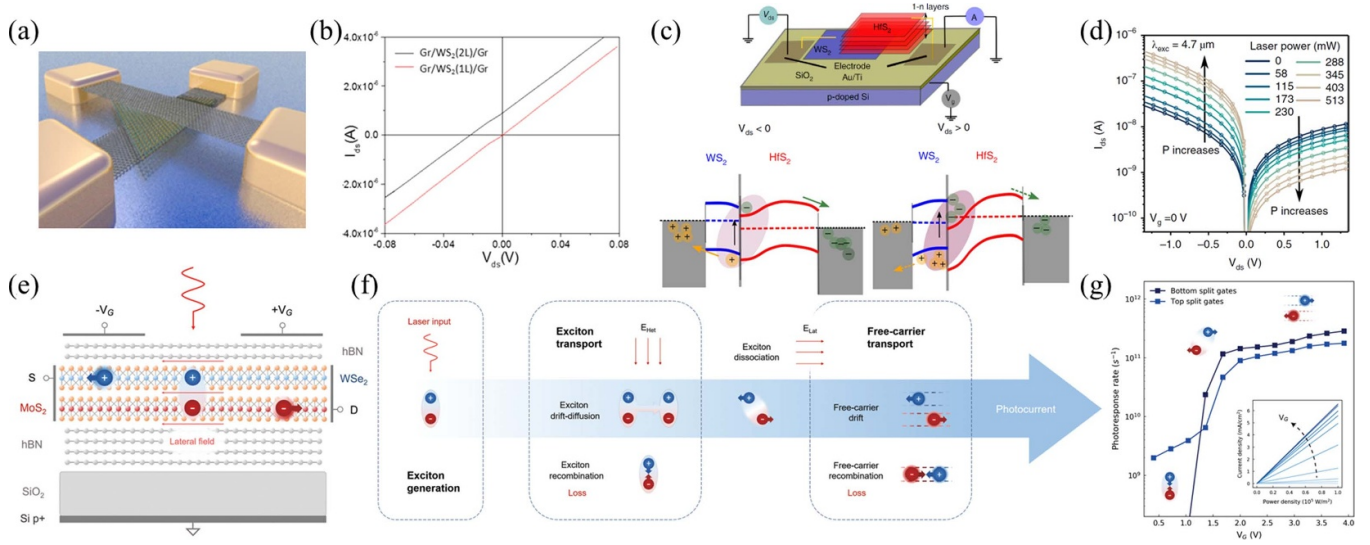
Figure 13. IX photodetectors. (a) Schematic diagram of the vertically sandwiched Gr/WS$_2$/Gr device. (b) Output curves of Gr/WS$_2$(2L)/Gr and Gr/WS$_2$(1L)/Gr photodetectors under 532 nm illumination with the back-gate of 80 V. (a) And (b) Reprinted with permission from [238]. Copyright (2018) American Chemical Society. (c) Schematic illustration of the WS$_2$/HfS$_2$ device structure and diagrams of the band alignment of the WS$_2$/HfS$_2$ photodetector under negative and positive voltages with charge extraction process. (d) I–V curve of the WS$_2$/HfS$_2$ photodetector under the excitation wavelength of 4.7 μm. (c) And (d) Adapted from [239], with permission from Springer Nature. (e) Schematic illustration of the top split-gate photodetector. (f) Schematic diagram of the three primary states of photocurrent evolution. (g) Photoresponse rate as a function of gate voltage. The inset shows the output current density as a function of input power density. (e)–(f) Reproduced from [240]. CC BY 3.0.

spatially separated, manifesting as positive and negative polarization distribution in the polarization-resolved PL mapping and cutline profiles (figure 12(c)). This distribution of σ^+ and σ^- emission shows a peak separation of 0.30 $\pm$ 0.02 μm, evidencing the robustness of VHE of IXs at room temperature, opening up practical implementation for developing valleytronic devices.

Furthermore, electrons and holes in different layers can also independently transport in the Hall bar device, demonstrating a gate-tunable valley transistor with regulable VHE magnitude and polarity [233]. In addition to being bound as IXs propagate in different transverse directions, the layer-dependent separation of electrons and holes allows for the isolation of opposite VHE contribution to the valley current (figure 12(d)). By modulating the light polarization through a set of a liquid crystal and polarizer, the Hall voltage can be detected under varying circularly polarized excitation (figure 12(e)). As shown in figure 12(f), the Hall voltage V_{H} displays a linear correlation with bias voltage V_x when subjected to circular polarization modulation, whereas its dependence on linear polarization modulation is negligible. Notably, the Hall voltages exhibit distinct polarity changes by varying the back-gate voltage, especially at -23.50 V and -28.25 V, where the corresponding linear slopes show opposite signs (figures 12(g) and (h)). This phenomenon stems from the electrically controllable valley-dependent band shifts [234], which enables a gate-tunable bipolar VHE, suggesting the potential application of valleytronic transistors with high ON/OFF ratios in valleytronic logic circuits.

5.3. Photodetectors

Beyond diffusion or transport throughout the entire heterostructure region, lateral electric fields further promote efficient charge dissociation of IXs. Coupled with their long exciton lifetimes that benefits carrier collection, these properties make them highly suitable for photodetector applications, enabling large photocurrents and responsivities [235–237]. For instance, the bilayer WS$_2$ photodetector exhibits a significantly increased photovoltaic effects compared with the monolayer WS$_2$ photodetector. Due to the relatively smaller binding energy of IXs compared to intralayer excitons, the Gr/WS$_2$(2L)/Gr device exhibits much higher short-circuit current ($I_{\mathrm{sc}} = 9 \times 10^{-7}$ A) and open-circuit voltage ($V_{\mathrm{oc}} = 22$ mV) than that of Gr/WS$_2$(1L)/Gr device (figures 13(a) and (b)) [238]. Apart from the increased light absorbance in bilayer WS$_2$, the relatively low binding energy of IXs enhance the exciton dissociation, while their nanosecond lifetimes contribute a higher number of free charge carriers, thereby increasing the photocurrent.

Notably, the relatively small interlayer coupling transition energy of the TMD heterobilayers enables infrared photoresponse. Recently, numerous studies have reported infrared photodetectors based on IXs in 2D layered vdW heterostructures [239, 241–247]. The significant photovoltaic effect suggests that IXs preferentially accumulate at the junction interface. By applying lateral voltage between the drain and source, IXs can be dissociated into free carriers, contributing to the photocurrent. As shown in figure 13(c),

negative voltages promote efficient charge extraction, facilitating the flow of electrons to HfS_2 and holes to WS_2, thus providing positive feedback to the photocurrent [239]. Conversely, in the positive voltage regime, the dissociated electrons and holes move against the applied electric filed, surmounting a higher energy barrier, resulting in photocurrent with negative feedback (figure 13(d)). Due to the enhanced oscillator strength of IXs in WS_2/HfS_2 heterostructures, these photodetectors exhibit high responsivies of approximately 10^3 A W^{-1}. Furthermore, these infrared photodetectors have been reported to exhibit gate-tunable photoresponse wavelengths and responsivities [239, 247]. To this end, this tunability enables spectral reconstruction, paving the way for the development of novel on-chip spectral imager with micron footprints.

Nonetheless, it is important to note that the operation speeds of most infrared photodetectors are limited to the millisecond to microsecond range. To address this response time limitation, Lopriore *et al* have developed ultrafast split-gate photodetectors with picosecond response times (figure 13(e)) [240]. This split-gate configuration allows for regulated exciton transport through the vertical electric field. In this design, gate voltages introduce substantial electrostatic potentials, forming lateral *p–n* junctions that promote efficient exciton dissociation into free-carrier driven by the lateral electric field (figure 13(f)), resulting in maximum responsivities of approximately 50 mA W^{-1}. Although top and bottom split-gate detectors exhibit slightly different photoresponse rate due to variations in electrostatic potential and lateral junction field distribution, both configurations demonstrate three distinct operational regimes: (1) IX recombination at low gate voltages, (2) IX dissociation at moderate field strengths, and (3) free-carrier drift for gate voltage exceeding 1.6 V (figure 13(g)). Furthermore, the photocurrent density shows a high degree of linearity with respect to the input density, paving the way for future photodetector arrays in artificial neural networks that require linear matrix-vector operations.

In this section, we have review the excitonic applications based on the manipulation of IX diffusion and transport, including the excitonic devices, valleytronic transistors and photodetectors. IXs can be electrically controlled with reconfigurable energy landscapes to guide their movement, enabling the development of all-optical excitonic transistors, diodes, and routers with high ON/OFF ratios. The in-plane electric fields further induce VHE to separate IXs into different valleys, promoting the innovation of valleytronic transistors. Besides, the efficient charge dissociation enhanced by lateral electric fields render IXs suitable for high-performance photodetectors, characterized by large photocurrents, high responsivities, tunable spectral responses and fast response times. Overall, advances in excitonic applications highlight the potential of IXs for next-generation excitonic applications and integrated on-chip devices, offering novel pathways for manipulating exciton transport and enhancing device performance across various domains.

6. Future perspectives

The study of IX propagation in TMD heterostructures offers a fertile platform for exploring unique physical phenomena and emerging innovative applications, holding great potential for revolutionizing optoelectronic technologies. The inherent spatially indirect nature provides IXs with permanent dipole moments and extended lifetimes, making them ideal candidates for long-range transport with controllable directionality. Coupled with the twist dynamics and valley-dependent physics, novel IX-based states can enable tunable exciton fluxes with emerging quantum phases, offering rich opportunities for exploring exotic phenomena and initiating technological advancements. As we mainly review the recent investigation delving into the fundamental principles, manipulation techniques and applications of IX diffusion and transport, transforming this fundamental understanding into practical devices necessitates addressing challenges and leveraging emerging opportunities. One significant challenge is the strict twist-angle homogeneity, which remains difficult for large-scale manufacturing for practical applications. As the size of moiré superlattices and depth of moiré potentials highly depends on the twist angle, how to achieve uniform moiré superlattice with minimized dielectric inhomogeneities and defects over mesoscopic scales remains challenging. The current fabrication method by exfoliating TMD monolayers and stacking them layer by layer can only produce heterostructures at the microscopic scale, where the inhomogenous strain and disorder are inevitable. Further bottom-up growth, like chemical vapor deposition may realize large-scale fabrication, but the precise control of twist angle in mesoscopic scale continues to be a challenge. Therefore, the innovative scalable fabrication methods are urgently required to produce high-quality vdW heterostructures with controlled interfaces and desired twist angles.

Additionally, both temporal and spatial resolutions of current spatiotemporal mapping techniques remain limited. Previous work has demonstrated that the formation time of IXs occurs on the sub-100 fs [35]. However, most imaging acquisitions are limited to timescales of several hundred picoseconds, which may hinder the in-depth comprehension of time-dependent spatial expansion of degenerate electron-hole states as the phase transition may occur at any time. Currently, the study of the exciton diffusion dynamics on ultrafast timescale is still constrained by the instrument response time, which require further improvement. Besides, current PL images of spatial exciton cloud distributions perform on a micrometer scale, while reports of local atomic registry within moiré superlattice usually lies at the nanometer scale, significantly below the diffraction limit of optical spectroscopies. Thus, the origin of moiré-trapped excitons and their migration between periodic moiré potentials should be better understood. Further research directions are expected to focus on the improvement of temporal and spatial resolutions.

Moreover, beyond conventional TMD heterostructures, the exploration of diffusion dynamics of easily access-

ible momentum-direct IXs in emerging vdW heterostructures presents exciting opportunities. As discussed above, IXs exhibit the longest diffusion length at twist angles of $0°$ or $60°$. However, the small twist angles facilitate the emergence of moiré potentials, which in turn impede IX diffusion and detrimental to long-range exciton transport. Therefore, the effective exciton transport necessitates the precise stacking of various monolayer TMDs, which always remains challenging and requires the second-harmonic generation measurement to accurately verify this twist angle. Thus, exploring novel 2D materials that can be randomly stacked with monolayer TMDs may lead to new systems capable of directly forming momentum-direct IXs and be conducive to IX transport. For instance, pervious work has demonstrated the tunable momentum-direct IXs in nL-InSe/2L-WS$_2$ heterostructures regardless of stacking alignment [71]; however, studies on their transport within these heterostructures are seldom discussed. Besides, other work has also reported long-distance charge transport over 5 μm in 2D perovskites, mediated by trap-induced exciton dissociation into long-lived and nonradiative electron-hole separated state, which can be described as a 'trapping-detrapping process' [248]. In addition, the incorporation of cross-dimensional materials may introduce novel exciton transport dynamics, such as the directional transport in mixed-dimensional heterostructures [249]. These findings suggest that integration of materials with various types and dimensions could potentially lead to exotic phenomena with innovative concepts and novel mechanisms, enabling IXs to travel long distances and broadening the range of tunable properties and functionalities.

Lastly, excitonic applications of TMD heterostructures are still in their infancy. The ability to manipulate IX propagation by external stimuli, like electric fields, lays the groundwork for developing excitonic circuits and devices. Considering the significant valley Zeeman effect and effective magnetic control of valley polarization, the magnetic field manipulation emerges as a promising approach to achieve near-unity valley-polarized IXs. Taking advantage of their valley-contrasting nature and long valley polarization lifetime, IXs show great promise for valleytronic transistors and memory devices under the magnetic field control. However, this particular method of manipulation has been rarely explored and warrants further exploration and detailed investigation. In addition, alternative strategies, such as fluorescence blinking [250], may also regulate exciton diffusion, potentially inducing diffusion blinking between different exciton states. Moreover, current exploration of these devices primarily focuses on free IX transport. A deeper understanding of excitonic many-body complexes, such as the charged or hybrid states, quadrupolar IXs or different phases under certain conditions, is crucial, holding potential for macroscopic exciton superfluidity and condensation. Currently, the understanding of the mechanisms governing the transport of these complex many-particle compounds, as well as their valley coherence, is still lacking. Besides, the operational speeds of these devices are not yet on par with the conventional electronic circuits. Therefore, more efforts should be dedicated to study the intrinsic diffusion dynamics and

practical application of these exciton complexes, and improve the performance of these devices.

The field of IX diffusion and transport in TMD heterostructures is brimming with great potential, providing a compelling platform for fundamental research and technological innovation. Beyond TMD heterostructures, we expect the integration of new materials and novel device structures further expand the current discoveries in vdW heterostructures. Advancements in material selection, precise construction methods, progressive characterization strategies, and performance optimization propel IXs to the forefront of next-generation optoelectronics, paving the way for a new era of excitonic manipulation and applications with unprecedented capabilities.

ORCID iDs

Yingying Chen ⬤ https://orcid.org/0000-0003-4519-5836
Dehui Li ⬤ https://orcid.org/0000-0002-5945-220X

References

[1] Wagner K *et al* 2021 Nonclassical exciton diffusion in monolayer WSe$_2$ *Phys. Rev. Lett.* **127** 076801
[2] Rosati R, Wagner K, Brem S, Perea-Causín R, Ziegler J D, Zipfel J, Taniguchi T, Watanabe K, Chernikov A and Malic E 2021 Non-equilibrium diffusion of dark excitons in atomically thin semiconductors *Nanoscale* **13** 19966–72
[3] Cheng G, Li B, Jin Z, Zhang M and Wang J 2021 Observation of diffusion and drift of the negative trions in monolayer WS$_2$ *Nano Lett.* **21** 6314–20
[4] Zipfel J *et al* 2020 Exciton diffusion in monolayer semiconductors with suppressed disorder *Phys. Rev. B* **101** 115430
[5] Yu Y, Yu Y, Li G, Puretzky A A, Geohegan D B and Cao L 2020 Giant enhancement of exciton diffusivity in two-dimensional semiconductors *Sci. Adv.* **6** eabb4823
[6] Uddin S Z, Kim H, Lorenzon M, Yeh M, Lien D H, Barnard E S, Htoon H, Weber-Bargioni A and Javey A 2020 Neutral exciton diffusion in monolayer MoS$_2$ *ACS Nano* **14** 13433–40
[7] Hao S, Bellus M Z, He D, Wang Y and Zhao H 2020 Controlling exciton transport in monolayer MoSe$_2$ by dielectric screening *Nanoscale Horiz.* **5** 139–43
[8] Kulig M, Zipfel J, Nagler P, Blanter S, Schuller C, Korn T, Paradiso N, Glazov M M and Chernikov A 2018 Exciton diffusion and halo effects in monolayer semiconductors *Phys. Rev. Lett.* **120** 207401
[9] Cadiz F *et al* 2018 Exciton diffusion in WSe$_2$ monolayers embedded in a van der Waals heterostructure *Appl. Phys. Lett.* **112** 152106

[10] Tan C *et al* 2017 Recent advances in ultrathin two-dimensional nanomaterials *Chem. Rev.* **117** 6225–331

[11] Zheng W, Jiang Y, Hu X, Li H, Zeng Z, Wang X and Pan A 2018 Light emission properties of 2D transition metal dichalcogenides: fundamentals and applications *Adv. Opt. Mater.* **6** 1800420

[12] Manzeli S, Ovchinnikov D, Pasquier D, Yazyev O V and Kis A 2017 2D transition metal dichalcogenides *Nat. Rev. Mater.* **2** 17033

[13] Liu G B, Xiao D, Yao Y, Xu X and Yao W 2015 Electronic structures and theoretical modelling of two-dimensional group-VIB transition metal dichalcogenides *Chem. Soc. Rev.* **44** 2643–63

[14] Wang Q H, Kalantar-Zadeh K, Kis A, Coleman J N and Strano M S 2012 Electronics and optoelectronics of two-dimensional transition metal dichalcogenides *Nat. Nanotechnol.* **7** 699–712

[15] Nguyen-Truong H T 2022 Exciton binding energy and screening length in two-dimensional semiconductors *Phys. Rev.* B **105** L201407

[16] Florian M, Hartmann M, Steinhoff A, Klein J, Holleitner A W, Finley J J, Wehling T O, Kaniber M and Gies C 2018 The dielectric impact of layer distances on exciton and trion binding energies in van der Waals heterostructures *Nano Lett.* **18** 2725–32

[17] Chernikov A, van der Zande A M, Hill H M, Rigosi A F, Velauthapillai A, Hone J and Heinz T F 2015 Electrical tuning of exciton binding energies in monolayer WS_2 *Phys. Rev. Lett.* **115** 126802

[18] Chernikov A, Berkelbach T C, Hill H M, Rigosi A, Li Y, Aslan O B, Reichman D R, Hybertsen M S and Heinz T F 2014 Exciton binding energy and nonhydrogenic Rydberg series in monolayer WS_2 *Phys. Rev. Lett.* **113** 076802

[19] Pei J, Yang J, Yildirim T, Zhang H and Lu Y 2019 Many-body complexes in 2D semiconductors *Adv. Mater.* **31** e1706945

[20] Chen S Y, Goldstein T, Taniguchi T, Watanabe K and Yan J 2018 Coulomb-bound four- and five-particle intervalley states in an atomically-thin semiconductor *Nat. Commun.* **9** 3717

[21] Li Z *et al* 2019 Direct observation of gate-tunable dark trions in monolayer WSe_2 *Nano Lett.* **19** 6886–93

[22] Van Tuan D, Shi S-F, Xu X, Crooker S A and Dery H 2022 Six-body and eight-body exciton states in monolayer WSe_2 *Phys. Rev. Lett.* **129** 076801

[23] Xu X, Yao W, Xiao D and Heinz T F 2014 Spin and pseudospins in layered transition metal dichalcogenides *Nat. Phys.* **10** 343–50

[24] Schaibley J R, Yu H, Clark G, Rivera P, Ross J S, Seyler K L, Yao W and Xu X 2016 Valleytronics in 2D materials *Nat. Rev. Mater.* **1** 16055

[25] Vitale S A, Nezich D, Varghese J O, Kim P, Gedik N, Jarillo-Herrero P, Xiao D and Rothschild M 2018 Valleytronics: opportunities, challenges, and paths forward *Small* **14** e1801483

[26] Kum H, Lee D, Kong W, Kim H, Park Y, Kim Y, Baek Y, Bae S-H, Lee K and Kim J 2019 Epitaxial growth and layer-transfer techniques for heterogeneous integration of materials for electronic and photonic devices *Nat. Electron.* **2** 439–50

[27] Dong R and Kuljanishvili I 2017 Review article: progress in fabrication of transition metal dichalcogenides heterostructure systems *J. Vac. Sci. Technol.* B **35** 030803

[28] Wang S, Cui X, Jian C, Cheng H, Niu M, Yu J, Yan J and Huang W 2021 Stacking-engineered heterostructures in transition metal dichalcogenides *Adv. Mater.* **33** e2005735

[29] Guo H W, Hu Z, Liu Z B and Tian J G 2020 Stacking of 2D materials *Adv. Funct. Mater.* **31** 2007810

[30] Liu Y, Huang Y and Duan X 2019 Van der Waals integration before and beyond two-dimensional materials *Nature* **567** 323–33

[31] Novoselov K S, Mishchenko A, Carvalho A and Castro Neto A H 2016 2D materials and van der Waals heterostructures *Science* **353** aac9439

[32] Jin C, Ma E Y, Karni O, Regan E C, Wang F and Heinz T F 2018 Ultrafast dynamics in van der Waals heterostructures *Nat. Nanotechnol.* **13** 994–1003

[33] Bradac C, Xu Z Q and Aharonovich I 2021 Quantum energy and charge transfer at two-dimensional interfaces *Nano Lett.* **21** 1193–204

[34] Hong X, Kim J, Shi S F, Zhang Y, Jin C, Sun Y, Tongay S, Wu J, Zhang Y and Wang F 2014 Ultrafast charge transfer in atomically thin MoS_2/WS_2 heterostructures *Nat. Nanotechnol.* **9** 682–6

[35] Schmitt D *et al* 2022 Formation of moiré interlayer excitons in space and time *Nature* **608** 499–503

[36] Tang J, Zheng Y, Jiang K, You Q, Yin Z, Xie Z, Li H, Han C, Zhang X and Shi Y 2023 Interlayer exciton dynamics of transition metal dichalcogenide heterostructures under electric fields *Nano Res.* **17** 4555–72

[37] Jiang Y, Chen S, Zheng W, Zheng B and Pan A 2021 Interlayer exciton formation, relaxation, and transport in TMD van der Waals heterostructures *Light Sci. Appl.* **10** 72

[38] Regan E C, Wang D, Paik E Y, Zeng Y, Zhang L, Zhu J, MacDonald A H, Deng H and Wang F 2022 Emerging exciton physics in transition metal dichalcogenide heterobilayers *Nat. Rev. Mater.* **7** 778–95

[39] Liu Y, Elbanna A, Gao W, Pan J, Shen Z and Teng J 2022 Interlayer excitons in transition metal dichalcogenide semiconductors for 2D optoelectronics *Adv. Mater.* **34** 2107138

[40] Baranowski M *et al* 2017 Probing the interlayer exciton physics in a MoS_2/$MoSe_2$/MoS_2 van der Waals heterostructure *Nano Lett.* **17** 6360–5

[41] Jiang C, Xu W, Rasmita A, Huang Z, Li K, Xiong Q and Gao W B 2018 Microsecond dark-exciton valley polarization memory in two-dimensional heterostructures *Nat. Commun.* **9** 753

[42] Robert C *et al* 2016 Exciton radiative lifetime in transition metal dichalcogenide monolayers *Phys. Rev.* B **93** 205423

[43] Karni O *et al* 2019 Infrared interlayer exciton emission in MoS_2/WSe_2 heterostructures *Phys. Rev. Lett.* **123** 247402

[44] Jauregui L A *et al* 2019 Electrical control of interlayer exciton dynamics in atomically thin heterostructures *Science* **366** 870–5

[45] Butov L V 2017 Excitonic devices *Superlattices Microstruct.* **108** 2–26

[46] Butov L V 2023 *Semiconductors and Semimetals* vol 112, ed P B Deotare and Z Mi (Elsevier) pp 145–87

[47] Liu Y, Zhu Y, Yan Z, Bai R, Zhang X, Ren Y, Cheng X, Ma H and Jiang C 2024 Excitonic devices based on two-dimensional transition metal dichalcogenides van der Waals heterostructures *Front. Chem. Sci. Eng.* **18** 16

[48] Sun X *et al* 2024 Twisted van der Waals quantum materials: fundamentals, tunability, and applications *Chem. Rev.* **124** 1992–2079

[49] Du L, Molas M R, Huang Z, Zhang G, Wang F and Sun Z 2023 Moiré photonics and optoelectronics *Science* **379** eadg0014

[50] Nuckolls K P and Yazdani A 2024 A microscopic perspective on moiré materials *Nat. Rev. Mater.* **9** 460–80

[51] Choi J *et al* 2020 Moiré potential impedes interlayer exciton diffusion in van der Waals heterostructures *Sci. Adv.* **6** eaba8866

[52] Li Z *et al* 2021 Interlayer exciton transport in $MoSe_2$/WSe_2 heterostructures *ACS Nano* **15** 1539–47

[53] Rivera P, Yu H, Seyler K L, Wilson N P, Yao W and Xu X 2018 Interlayer valley excitons in heterobilayers of transition metal dichalcogenides *Nat. Nanotechnol.* **13** 1004–15

[54] Rivera P, Seyler K L, Yu H, Schaibley J R, Yan J, Mandrus D G, Yao W and Xu X 2016 Valley-polarized exciton dynamics in a 2D semiconductor heterostructure *Science* **351** 688–91

[55] Mak K F, McGill K L, Park J and McEuen P L 2014 The valley Hall effect in MoS$_2$ transistors *Science* **344** 1489–92

[56] Xiao D, Liu G B, Feng W, Xu X and Yao W 2012 Coupled spin and valley physics in monolayers of MoS$_2$ and other group-VI dichalcogenides *Phys. Rev. Lett.* **108** 196802

[57] Ciarrocchi A, Tagarelli F, Avsar A and Kis A 2022 Excitonic devices with van der Waals heterostructures: valleytronics meets twistronics *Nat. Rev. Mater.* **7** 449–64

[58] Perea-Causin R, Erkensten D, Fitzgerald J M, Thompson J J P, Rosati R, Brem S and Malic E 2022 Exciton optics, dynamics, and transport in atomically thin semiconductors *APL Mater.* **10** 100701

[59] Qi P *et al* 2022 Molding 2D exciton flux toward room temperature excitonic devices *Adv. Mater. Technol.* **7** 2200032

[60] Lee H, Kim Y B, Ryu J W, Kim S, Bae J, Koo Y, Jang D and Park K-D 2023 Recent progress of exciton transport in two-dimensional semiconductors *Nano Converg.* **10** 57

[61] Policht V R *et al* 2023 Time-domain observation of interlayer exciton formation and thermalization in a MoSe$_2$/WSe$_2$ heterostructure *Nat. Commun.* **14** 7273

[62] Fang H, Battaglia C, Carraro C, Nemsak S, Ozdol B, Kang J S, Bechtel H A, Desai S B, Kronast F and Unal A A 2014 Strong interlayer coupling in van der Waals heterostructures built from single-layer chalcogenides *Proc. Natl Acad. Sci.* **111** 6198–202

[63] Rivera P *et al* 2015 Observation of long-lived interlayer excitons in monolayer MoSe$_2$-WSe$_2$ heterostructures *Nat. Commun.* **6** 6242

[64] Chen H *et al* 2016 Ultrafast formation of interlayer hot excitons in atomically thin MoS$_2$/WS$_2$ heterostructures *Nat. Commun.* **7** 12512

[65] Alexeev E M *et al* 2017 Imaging of interlayer coupling in van der Waals heterostructures using a bright-field optical microscope *Nano Lett.* **17** 5342–9

[66] Nagler P *et al* 2017 Interlayer exciton dynamics in a dichalcogenide monolayer heterostructure *2D Mater.* **4** 025112

[67] Wang K *et al* 2016 Interlayer coupling in twisted WSe$_2$/WS$_2$ bilayer heterostructures revealed by optical spectroscopy *ACS Nano* **10** 6612–22

[68] Choi C *et al* 2018 Enhanced interlayer neutral excitons and trions in trilayer van der Waals heterostructures *npj 2D Mater. Appl.* **2** 30

[69] Mouri S, Zhang W, Kozawa D, Miyauchi Y, Eda G and Matsuda K 2017 Thermal dissociation of inter-layer excitons in MoS$_2$/MoSe$_2$ hetero-bilayers *Nanoscale* **9** 6674–9

[70] Okada M *et al* 2018 Direct and indirect interlayer excitons in a van der Waals heterostructure of hBN/WS$_2$/MoS$_2$/hBN *ACS Nano* **12** 2498–505

[71] Ubrig N *et al* 2020 Design of van der Waals interfaces for broad-spectrum optoelectronics *Nat. Mater.* **19** 299–304

[72] Tan Q, Rasmita A, Li S, Liu S, Huang Z, Xiong Q, Yang S A, Novoselov K S and Gao W-B 2021 Layer-engineered interlayer excitons *Sci. Adv.* **7** eabh0863

[73] Barre E *et al* 2022 Optical absorption of interlayer excitons in transition-metal dichalcogenide heterostructures *Science* **376** 406–10

[74] Nayak P K *et al* 2017 Probing evolution of twist-angle-dependent interlayer excitons in MoSe$_2$/WSe$_2$ van der Waals heterostructures *ACS Nano* **11** 4041–50

[75] Liu K, Zhang L, Cao T, Jin C, Qiu D, Zhou Q, Zettl A, Yang P, Louie S G and Wang F 2014 Evolution of interlayer coupling in twisted molybdenum disulfide bilayers *Nat. Commun.* **5** 4966

[76] Ji Z *et al* 2017 Robust stacking-independent ultrafast charge transfer in MoS$_2$/WS$_2$ bilayers *ACS Nano* **11** 12020–6

[77] Zhu H, Wang J, Gong Z, Kim Y D, Hone J and Zhu X Y 2017 Interfacial charge transfer circumventing momentum mismatch at two-dimensional van der Waals heterojunctions *Nano Lett.* **17** 3591–8

[78] Kunstmann J *et al* 2018 Momentum-space indirect interlayer excitons in transition-metal dichalcogenide van der Waals heterostructures *Nat. Phys.* **14** 801–5

[79] Yang W *et al* 2018 Interlayer interactions in 2D WS$_2$/MoS$_2$ heterostructures monolithically grown by *in situ* physical vapor deposition *Nanoscale* **10** 22927–36

[80] Geng W T, Wang V, Lin J B, Ohno T and Nara J 2020 Angle dependence of interlayer coupling in twisted transition metal dichalcogenide heterobilayers *J. Phys. Chem.* C **125** 1048–53

[81] Liao M *et al* 2020 Precise control of the interlayer twist angle in large scale MoS$_2$ homostructures *Nat. Commun.* **11** 2153

[82] Mak K F and Shan J 2022 Semiconductor moiré materials *Nat. Nanotechnol.* **17** 686–95

[83] Huang D, Choi J, Shih C K and Li X 2022 Excitons in semiconductor moiré superlattices *Nat. Nanotechnol.* **17** 227–38

[84] Zhu Y, Fang W-H, Rubio A, Long R and Prezhdo O V 2022 The twist angle has weak influence on charge separation and strong influence on recombination in the MoS$_2$/WS$_2$ bilayer: *ab initio* quantum dynamics *J. Mater. Chem.* A **10** 8324–33

[85] Montblanch A R P *et al* 2021 Confinement of long-lived interlayer excitons in WS$_2$/WSe$_2$ heterostructures *Commun. Phys.* **4** 119

[86] Miller B, Steinhoff A, Pano B, Klein J, Jahnke F, Holleitner A and Wurstbauer U 2017 Long-lived direct and indirect interlayer excitons in van der Waals heterostructures *Nano Lett.* **17** 5229–37

[87] Laikhtman B and Rapaport R 2009 Exciton correlations in coupled quantum wells and their luminescence blue shift *Phys. Rev.* B **80** 195313

[88] Ivanov A L 2002 Quantum diffusion of dipole-oriented indirect excitons in coupled quantum wells *Europhys. Lett.* **59** 586–91

[89] Wang Z, Chiu Y H, Honz K, Mak K F and Shan J 2018 Electrical tuning of interlayer exciton gases in WSe$_2$ bilayers *Nano Lett.* **18** 137–43

[90] Unuchek D, Ciarrocchi A, Avsar A, Sun Z, Watanabe K, Taniguchi T and Kis A 2019 Valley-polarized exciton currents in a van der Waals heterostructure *Nat. Nanotechnol.* **14** 1104–9

[91] Ciarrocchi A, Unuchek D, Avsar A, Watanabe K, Taniguchi T and Kis A 2019 Polarization switching and electrical control of interlayer excitons in two-dimensional van der Waals heterostructures *Nat. Photon.* **13** 131–6

[92] Joe A Y *et al* 2021 Electrically controlled emission from singlet and triplet exciton species in atomically thin light-emitting diodes *Phys. Rev.* B **103** L161411

[93] Lin K-Q *et al* 2023 Ultraviolet interlayer excitons in bilayer WSe$_2$ *Nat. Nanotechnol.* **19** 196–201

[94] Yang D, Liang J, Wu J, Xiao Y, Dadap J I, Watanabe K, Taniguchi T and Ye Z 2024 Non-volatile electrical

polarization switching via domain wall release in 3R-MoS$_2$ bilayer *Nat. Commun.* **15** 1389

[95] Wilson N P, Yao W, Shan J and Xu X 2021 Excitons and emergent quantum phenomena in stacked 2D semiconductors *Nature* **599** 383–92

[96] Sun X, Malic E and Lu Y 2024 Dipolar many-body complexes and their interactions in stacked 2D heterobilayers *Nat. Rev. Phys.* **6** 439–54

[97] Zhao Y *et al* 2022 Interlayer exciton complexes in bilayer MoS$_2$ *Phys. Rev.* B **105** L041411

[98] Huang Z *et al* 2022 Spatially indirect intervalley excitons in bilayer WSe$_2$ *Phys. Rev.* B **105** L041409

[99] Scuri G *et al* 2020 Electrically tunable valley dynamics in twisted WSe$_2$/WSe$_2$ bilayers *Phys. Rev. Lett.* **124** 217403

[100] Zhang L, Gogna R, Burg G W, Horng J, Paik E, Chou Y-H, Kim K, Tutuc E and Deng H 2019 Highly valley-polarized singlet and triplet interlayer excitons in van der Waals heterostructure *Phys. Rev.* B **100** 041402

[101] Hanbicki A T, Chuang H J, Rosenberger M R, Hellberg C S, Sivaram S V, McCreary K M, Mazin I I and Jonker B T 2018 Double indirect interlayer exciton in a MoSe$_2$/WSe$_2$ van der Waals heterostructure *ACS Nano* **12** 4719–26

[102] Hu Y, Wen X, Lin J, Yao W, Chen Y, Li J, Chen S, Wang L, Xu W and Li D 2023 All-optical valley polarization switch via controlling spin-triplet and spin-singlet interlayer exciton emission in WS$_2$/WSe$_2$ heterostructure *Nano Lett.* **23** 6581–7

[103] Ye T, Li Y, Li J, Shen H, Ren J, Ning C Z and Li D 2022 Nonvolatile electrical switching of optical and valleytronic properties of interlayer excitons *Light Sci. Appl.* **11** 23

[104] Jin C *et al* 2019 Observation of moiré excitons in WSe$_2$/WS$_2$ heterostructure superlattices *Nature* **567** 76–80

[105] Tran K *et al* 2019 Evidence for moiré excitons in van der Waals heterostructures *Nature* **567** 71–75

[106] Yu H, Liu G-B, Tang J, Xu X and Yao W 2017 Moiré excitons: from programmable quantum emitter arrays to spin-orbit–coupled artificial lattices *Sci. Adv.* **3** e1701696

[107] Zhang C, Chuu C-P, Ren X, Li M-Y, Li L-J, Jin C, Chou M-Y and Shih C-K 2017 Interlayer couplings, moiré; patterns, and 2D electronic superlattices in MoS$_2$/WSe$_2$ hetero-bilayers *Sci. Adv.* **3** e1601459

[108] Guo H, Zhang X and Lu G 2020 Shedding light on moiré excitons: a first-principles perspective *Sci. Adv.* **6** eabc5638

[109] Carr S, Fang S and Kaxiras E 2020 Electronic-structure methods for twisted moiré layers *Nat. Rev. Mater.* **5** 748–63

[110] Seyler K L, Rivera P, Yu H, Wilson N P, Ray E L, Mandrus D G, Yan J, Yao W and Xu X 2019 Signatures of moiré-trapped valley excitons in MoSe$_2$/WSe$_2$ heterobilayers *Nature* **567** 66–70

[111] Ribeiro-Palau R, Zhang C, Watanabe K, Taniguchi T, Hone J and Dean C R 2018 Twistable electronics with dynamically rotatable heterostructures *Science* **361** 690–3

[112] Zhao S *et al* 2023 Excitons in mesoscopically reconstructed moiré heterostructures *Nat. Nanotechnol.* **18** 572–9

[113] Angeli M and MacDonald A H 2021 Gamma valley transition metal dichalcogenide moiré bands *Proc. Natl Acad. Sci. USA* **118** e2021826118

[114] Li H *et al* 2021 Imaging moiré flat bands in three-dimensional reconstructed WSe$_2$/WS$_2$ superlattices *Nat. Mater.* **20** 945–50

[115] Shabani S, Halbertal D, Wu W, Chen M, Liu S, Hone J, Yao W, Basov D N, Zhu X and Pasupathy A N 2021 Deep moiré potentials in twisted transition metal dichalcogenide bilayers *Nat. Phys.* **17** 720–5

[116] Lin B-H *et al* 2023 Remarkably deep moiré potential for intralayer excitons in MoSe$_2$/MoS$_2$ twisted heterobilayers *Nano Lett.* **23** 1306–12

[117] Liu Y *et al* 2024 Exciton localization modulated by ultradeep moiré potential in twisted bilayer γ-graphdiyne *J. Am. Chem. Soc.* **146** 14593–9

[118] Geng W T, Wang V, Liu Y C, Ohno T and Nara J 2020 Moiré potential, lattice corrugation, and band gap spatial variation in a twist-free MoTe$_2$/MoS$_2$ heterobilayer *J. Phys. Chem. Lett.* **11** 2637–46

[119] Naik M H *et al* 2022 Intralayer charge-transfer moiré excitons in van der Waals superlattices *Nature* **609** 52–57

[120] Baek H, Brotons-Gisbert M, Koong Z X, Campbell A, Rambach M, Watanabe K, Taniguchi T and Gerardot B D 2020 Highly energy-tunable quantum light from moiré-trapped excitons *Sci. Adv.* **6** eaba8526

[121] Jin C *et al* 2019 Identification of spin, valley and moiré quasi-angular momentum of interlayer excitons *Nat. Phys.* **15** 1140–4

[122] Brotons-Gisbert M, Baek H, Molina-Sanchez A, Campbell A, Scerri E, White D, Watanabe K, Taniguchi T, Bonato C and Gerardot B D 2020 Spin-layer locking of interlayer excitons trapped in moiré potentials *Nat. Mater.* **19** 630–6

[123] Blundo E *et al* 2024 Localisation-to-delocalisation transition of moiré excitons in WSe$_2$/MoSe$_2$ heterostructures *Nat. Commun.* **15** 1057

[124] Zhang L *et al* 2020 Twist-angle dependence of moiré excitons in WS$_2$/MoSe$_2$ heterobilayers *Nat. Commun.* **11** 5888

[125] Choi J *et al* 2021 Twist angle-dependent interlayer exciton lifetimes in van der Waals heterostructures *Phys. Rev. Lett.* **126** 047401

[126] Dai D *et al* 2024 Twist angle–dependent valley polarization switching in heterostructures *Sci. Adv.* **10** eado1281

[127] Wu B *et al* 2022 Evidence for moiré intralayer excitons in twisted WSe$_2$/WSe$_2$ homobilayer superlattices *Light Sci. Appl.* **11** 166

[128] Fang H, Lin Q, Zhang Y, Thompson J, Xiao S, Sun Z, Malic E, Dash S P and Wieczorek W 2023 Localization and interaction of interlayer excitons in MoSe$_2$/WSe$_2$ heterobilayers *Nat. Commun.* **14** 6910

[129] Tan Q, Rasmita A, Zhang Z, Novoselov K S and W-b G 2022 Signature of cascade transitions between interlayer excitons in a moiré superlattice *Phys. Rev. Lett.* **129** 247401

[130] Ge C, Zhang D, Xiao F, Zhao H, He M, Huang L, Hou S, Tong Q, Pan A and Wang X 2023 Observation and modulation of high-temperature moiré-locale excitons in van der Waals heterobilayers *ACS Nano* **17** 16115–22

[131] Alexeev E M *et al* 2019 Resonantly hybridized excitons in moiré superlattices in van der Waals heterostructures *Nature* **567** 81–86

[132] Villafane V, Kremser M, Huebner R, Petric M M, Wilson N P, Stier A V, Mueller K, Florian M, Steinhoff A and Finley J J 2023 Twist-dependent intra- and interlayer excitons in moiré acute accent MoSe$_2$ homobilayers *Phys. Rev. Lett.* **130** 026901

[133] Zhao S *et al* 2024 Hybrid moiré excitons and trions in twisted MoTe$_2$-MoSe$_2$ heterobilayers *Nano Lett.* **24** 4917–23

[134] Dandu M, Gupta G, Dasika P, Watanabe K, Taniguchi T and Majumdar K 2022 Electrically tunable localized versus delocalized intralayer moiré excitons and trions in a twisted MoS$_2$ bilayer *ACS Nano* **16** 8983–92

[135] Shi B-B, Tao G-Y, Dai Y-C, He X, Lin F, Zhang H and Fang Z-Y 2022 Exciton moiré potential in twisted WSe$_2$ homobilayers modulated by electric field *Acta Phys. Sin.* **71** 177301

[136] Wang X *et al* 2021 Moiré trions in MoSe$_2$/WSe$_2$ heterobilayers *Nat. Nanotechnol.* **16** 1208–13

[137] Liu E *et al* 2021 Signatures of moiré trions in WSe$_2$ heterobilayers *Nature* **594** 46–50

[138] Brotons-Gisbert M, Baek H, Campbell A, Watanabe K, Taniguchi T and Gerardot B D 2021 Moiré-trapped

interlayer trions in a charge-tunable $WSe_2/MoSe_2$ heterobilayer *Phys. Rev. X* **11** 031033

[139] Rapaport R, Chen G and Simon S H 2006 Nonlinear dynamics of a dense two-dimensional dipolar exciton gas *Phys. Rev. B* **73** 033319

[140] Sun Z, Ciarrocchi A, Tagarelli F, Gonzalez Marin J F, Watanabe K, Taniguchi T and Kis A 2022 Excitonic transport driven by repulsive dipolar interaction in a van der Waals heterostructure *Nat. Photon.* **16** 79–85

[141] Zhang L, Gu L, Ni R, Xie M, Park S, Jang H, Ma R, Taniguchi T, Watanabe K and Zhou Y 2024 Electrical control and transport of tightly bound interlayer excitons in a $MoSe_2/hBN/MoSe_2$ heterostructure *Phys. Rev. Lett.* **132** 216903

[142] Chen Y, Liu Z, Li J, Cheng X, Ma J, Wang H and Li D 2020 Robust interlayer coupling in two-dimensional perovskite/monolayer transition metal dichalcogenide heterostructures *ACS Nano* **14** 10258–64

[143] Yao W, Yang D, Chen Y, Hu J, Li J and Li D 2022 Layer-number engineered momentum-indirect interlayer excitons with large spectral tunability *Nano Lett.* **22** 7230–7

[144] Fowler-Gerace L H, Zhou Z, Szwed E A, Choksy D J and Butov L V 2024 Transport and localization of indirect excitons in a van der Waals heterostructure *Nat. Photon.* **18** 823–8

[145] Capogrosso-Sansone B, Söyler Ş G, Prokof'ev N and Svistunov B 2008 Monte Carlo study of the two-dimensional Bose-Hubbard model *Phys. Rev. A* **77** 015602

[146] Fisher M P A, Weichman P B, Grinstein G and Fisher D S 1989 Boson localization and the superfluid-insulator transition *Phys. Rev. B* **40** 546–70

[147] Calman E V, Fogler M M, Butov L V, Hu S, Mishchenko A and Geim A K 2018 Indirect excitons in van der Waals heterostructures at room temperature *Nat. Commun.* **9** 1895

[148] Wang P, He D, Wang Y, Zhang X, He X, He J and Zhao H 2021 Ultrafast interlayer charge transfer between bilayer ptse$_2$ and monolayer WS_2 *ACS Appl. Mater. Interfaces* **13** 57822–30

[149] Yuan L, Zheng B, Kunstmann J, Brumme T, Kuc A B, Ma C, Deng S, Blach D, Pan A and Huang L 2020 Twist-angle-dependent interlayer exciton diffusion in WS_2-WSe_2 heterobilayers *Nat. Mater.* **19** 617–23

[150] Qian W, Qi P, Dai Y, Shi B, Tao G, Liu H, Zhang X, Xiang D, Fang Z and Liu W 2024 Strongly localized moiré exciton in twisted homobilayers *Small* **20** 2305200

[151] Rossi A *et al* 2024 Anomalous interlayer exciton diffusion in WS_2/WSe_2 moiré heterostructure *ACS Nano* **18** 18202–10

[152] Wang J *et al* 2021 Diffusivity reveals three distinct phases of interlayer excitons in $MoSe_2/WSe_2$ heterobilayers *Phys. Rev. Lett.* **126** 106804

[153] Wietek E, Florian M, Goeser J, Taniguchi T, Watanabe K, Hoegele A, Glazov M M, Steinhoff A and Chernikov A 2024 Nonlinear and negative effective diffusivity of interlayer excitons in moiré-free heterobilayers *Phys. Rev. Lett.* **132** 016202

[154] Sun X, Zhu Y, Qin H, Liu B, Tang Y, Lu T, Rahman S, Yildirim T and Lu Y 2022 Enhanced interactions of interlayer excitons in free-standing heterobilayers *Nature* **610** 478–84

[155] Tagarelli F *et al* 2023 Electrical control of hybrid exciton transport in a van der Waals heterostructure *Nat. Photon.* **17** 615–21

[156] Fowler-Gerace L H, Choksy D J and Butov L V 2021 Voltage-controlled long-range propagation of indirect excitons in a van der Waals heterostructure *Phys. Rev. B* **104** 165302

[157] Peng R *et al* 2022 Long-range transport of 2D excitons with acoustic waves *Nat. Commun.* **13** 1334

[158] Wang X, Lin Z, Watanabe K, Taniguchi T, Yao W, Zhang S and Cui X 2024 Near-field coupling of interlayer excitons in $MoSe_2/WSe_2$ heterobilayers to surface plasmon polaritons *J. Chem. Phys.* **160** 141103

[159] Unuchek D, Ciarrocchi A, Avsar A, Watanabe K, Taniguchi T and Kis A 2018 Room-temperature electrical control of exciton flux in a van der Waals heterostructure *Nature* **560** 340–4

[160] Liu Y, Dini K, Tan Q, Liew T, Novoselov K S and Gao W 2020 Electrically controllable router of interlayer excitons *Sci. Adv.* **6** eaba1830

[161] Shanks D N, Mahdikhanysarvejahany F, Stanfill T G, Koehler M R, Mandrus D G, Taniguchi T, Watanabe K, LeRoy B J and Schaibley J R 2022 Interlayer exciton diode and transistor *Nano Lett.* **22** 6599–605

[162] Ju Q, Cai Q, Jian C, Hong W, Sun F, Wang B and Liu W 2024 Infrared interlayer excitons in twist-free $MoTe_2/MoS_2$ heterobilayers *Adv. Mater.* **36** 2404371

[163] Joe A Y *et al* 2024 Controlled interlayer exciton ionization in an electrostatic trap in atomically thin heterostructures *Nat. Commun.* **15** 6743

[164] Erkensten D, Brem S, Perea-Causin R and Malic E 2022 Microscopic origin of anomalous interlayer exciton transport in van der Waals heterostructures *Phys. Rev. Mater.* **6** 094006

[165] Yuan L, Zheng B, Zhao Q, Kempt R, Brumme T, Kuc A B B, Ma C, Deng S, Pan A and Huang L 2023 Strong dipolar repulsion of one-dimensional interfacial excitons in monolayer lateral heterojunctions *ACS Nano* **17** 15379–87

[166] Guo Z, Manser J S, Wan Y, Kamat P V and Huang L 2015 Spatial and temporal imaging of long-range charge transport in perovskite thin films by ultrafast microscopy *Nat. Commun.* **6** 7471

[167] Liu H, Wang C, Zuo Z, Liu D and Luo J 2020 Direct visualization of exciton transport in defective few-layer WS_2 by ultrafast microscopy *Adv. Mater.* **32** e1906540

[168] Deng S, Shi E, Yuan L, Jin L, Dou L and Huang L 2020 Long-range exciton transport and slow annihilation in two-dimensional hybrid perovskites *Nat. Commun.* **11** 664

[169] Knorr W, Brem S, Meneghini G and Malic E 2022 Exciton transport in a moiré potential: from hopping to dispersive regime *Phys. Rev. Mater.* **6** 124002

[170] Jin C *et al* 2021 Stripe phases in WSe_2/WS_2 moiré superlattices *Nat. Mater.* **20** 940–4

[171] Wang L *et al* 2020 Correlated electronic phases in twisted bilayer transition metal dichalcogenides *Nat. Mater.* **19** 861–6

[172] Xu Y, Liu S, Rhodes D A, Watanabe K, Taniguchi T, Hone J, Elser V, Mak K F and Shan J 2020 Correlated insulating states at fractional fillings of moiré superlattices *Nature* **587** 214–8

[173] Ghiotto A *et al* 2021 Quantum criticality in twisted transition metal dichalcogenides *Nature* **597** 345–9

[174] Shimazaki Y, Schwartz I, Watanabe K, Taniguchi T, Kroner M and Imamoglu A 2020 Strongly correlated electrons and hybrid excitons in a moiré heterostructure *Nature* **580** 472–7

[175] Tang Y *et al* 2020 Simulation of Hubbard model physics in WSe_2/WS_2 moiré superlattices *Nature* **579** 353–8

[176] Li T *et al* 2021 Continuous Mott transition in semiconductor moiré superlattices *Nature* **597** 350–4

[177] Miao S *et al* 2021 Strong interaction between interlayer excitons and correlated electrons in WSe_2/WS_2 moiré superlattice *Nat. Commun.* **12** 3608

[178] Gu J, Ma L, Liu S, Watanabe K, Taniguchi T, Hone J C, Shan J and Mak K F 2022 Dipolar excitonic insulator in a moiré lattice *Nat. Phys.* **18** 395–400

[179] Gao B *et al* 2024 Excitonic Mott insulator in a Bose-Fermi-Hubbard system of moiré WS$_2$/WSe$_2$ heterobilayer *Nat. Commun.* **15** 2305

[180] Deng S, Chu Y and Zhu Q 2022 Moiré exciton condensate: nonlinear dirac point, broken-symmetry bloch waves, and unusual optical selection rules *Phys. Rev.* B **106** 155410

[181] Guo H, Zhang X and Lu G 2022 Tuning moiré excitons in Janus heterobilayers for high-temperature Bose-Einstein condensation *Sci. Adv.* **8** eabp9757

[182] Shi Q *et al* 2022 Bilayer WSe$_2$ as a natural platform for interlayer exciton condensates in the strong coupling limit *Nat. Nanotechnol.* **17** 577–82

[183] Cao Y, Rodan-Legrain D, Park J M, Yuan N F Q, Watanabe K, Taniguchi T, Fernandes R M, Fu L and Jarillo-Herrero P 2021 Nematicity and competing orders in superconducting magic-angle graphene *Science* **372** 264–71

[184] Cao Y, Fatemi V, Fang S, Watanabe K, Taniguchi T, Kaxiras E and Jarillo-Herrero P 2018 Unconventional superconductivity in magic-angle graphene superlattices *Nature* **556** 43–50

[185] Balents L, Dean C R, Efetov D K and Young A F 2020 Superconductivity and strong correlations in moiré flat bands *Nat. Phys.* **16** 725–33

[186] Zeng Y, Xia Z, Dery R, Watanabe K, Taniguchi T, Shan J and Mak K F 2023 Exciton density waves in coulomb-coupled dual moiré lattices *Nat. Mater.* **22** 175–9

[187] Zhao W M, Zhu L, Nie Z, Li Q Y, Wang Q W, Dou L G, Hu J G, Xian L, Meng S and Li S C 2022 Moiré enhanced charge density wave state in twisted 1T-TiTe$_2$/1T-TiSe$_2$ heterostructures *Nat. Mater.* **21** 284–9

[188] Regan E C *et al* 2020 Mott and generalized wigner crystal states in WSe$_2$/WS$_2$ moiré superlattices *Nature* **579** 359–63

[189] Huang X *et al* 2021 Correlated insulating states at fractional fillings of the WS$_2$/WSe$_2$ moiré lattice *Nat. Phys.* **17** 715–9

[190] Li H *et al* 2021 Imaging two-dimensional generalized Wigner crystals *Nature* **597** 650–4

[191] Baek H, Brotons-Gisbert M, Campbell A, Vitale V, Lischner J, Watanabe K, Taniguchi T and Gerardot B D 2021 Optical read-out of coulomb staircases in a moiré superlattice via trapped interlayer trions *Nat. Nanotechnol.* **16** 1237–43

[192] Wang J, Ardelean J, Bai Y, Steinhoff A, Florian M, Jahnke F, Xu X, Kira M, Hone J and Zhu X Y 2019 Optical generation of high carrier densities in 2D semiconductor heterobilayers *Sci. Adv.* **5** eaax0145

[193] Brem S and Malic E 2023 Bosonic delocalization of dipolar moiré excitons *Nano Lett.* **23** 4627–33

[194] Choi J *et al* 2023 Fermi pressure and coulomb repulsion driven rapid hot plasma expansion in a van der Waals heterostructure *Nano Lett.* **23** 4399–405

[195] Bai Y, Li Y, Liu S, Guo Y, Pack J, Wang J, Dean C R, Hone J and Zhu X 2023 Evidence for exciton crystals in a 2D semiconductor heterotrilayer *Nano Lett.* **23** 11621–9

[196] Lian Z *et al* 2023 Quadrupolar excitons and hybridized interlayer Mott insulator in a trilayer moiré superlattice *Nat. Commun.* **14** 4604

[197] Li W, Hadjri Z, Devenica L M, Zhang J, Liu S, Hone J, Watanabe K, Taniguchi T, Rubio A and Srivastava A 2023 Quadrupolar-dipolar excitonic transition in a tunnel-coupled van der Waals heterotrilayer *Nat. Mater.* **22** 1478–84

[198] Yu L, Pistunova K, Hu J, Watanabe K, Taniguchi T and Heinz T F 2023 Observation of quadrupolar and dipolar excitons in a semiconductor heterotrilayer *Nat. Mater.* **22** 1485–91

[199] Xie Y *et al* 2023 Bright and dark quadrupolar excitons in the WSe$_2$/MoSe$_2$/WSe$_2$ heterotrilayer *Phys. Rev. Lett.* **131** 186901

[200] Liu H *et al* 2023 Direct visualization of dark interlayer exciton transport in moiré superlattices *Nano Lett.* **24** 339–46

[201] Fu Y, He D, He J, Bian A, Zhang L, Liu S, Wang Y and Zhao H 2019 Effect of dielectric environment on excitonic dynamics in monolayer WS$_2$ *Adv. Mater. Interfaces* **6** 1901307

[202] Raja A *et al* 2019 Dielectric disorder in two-dimensional materials *Nat. Nanotechnol.* **14** 832–7

[203] Li Z, Cordovilla Leon D F, Lee W, Datta K, Lyu Z, Hou J, Taniguchi T, Watanabe K, Kioupakis E and Deotare P B 2021 Dielectric engineering for manipulating exciton transport in semiconductor monolayers *Nano Lett.* **21** 8409–17

[204] Ajayi O A *et al* 2017 Approaching the intrinsic photoluminescence linewidth in transition metal dichalcogenide monolayers *2D Mater.* **4** 031011

[205] Raja A *et al* 2017 Coulomb engineering of the bandgap and excitons in two-dimensional materials *Nat. Commun.* **8** 15251

[206] Kamban H C and Pedersen T G 2020 Interlayer excitons in van der Waals heterostructures: binding energy, stark shift, and field-induced dissociation *Sci. Rep.* **10** 5537

[207] Rosati R *et al* 2023 Interface engineering of charge-transfer excitons in 2D lateral heterostructures *Nat. Commun.* **14** 2438

[208] Bondarev I V and Vladimirova M R 2018 Complexes of dipolar excitons in layered quasi-two-dimensional nanostructures *Phys. Rev.* B **97** 165419

[209] Van der Donck M and Peeters F M 2018 Interlayer excitons in transition metal dichalcogenide heterostructures *Phys. Rev.* B **98** 115104

[210] Latini S, Winther K T, Olsen T and Thygesen K S 2017 Interlayer excitons and band alignment in MoS$_2$/hBN/WSe$_2$ van der Waals heterostructures *Nano Lett.* **17** 938–45

[211] Wu B, Xie X, Chen J, Li S, Ding J, He J, Liu Z and Liu Y 2024 Optical microcavity-induced moiré exciton localization in twisted WSe$_2$ homobilayer *Adv. Funct. Mater.* **34** 2402493

[212] Hou Y and Yu H 2024 Dipolar interactions enhanced by two-dimensional dielectric screening in few-layer van der Waals structures *2D Mater.* **11** 025019

[213] Goetting N, Lohof F and Gies C 2022 Moiré-Bose-Hubbard model for interlayer excitons in twisted transition metal dichalcogenide heterostructures *Phys. Rev.* B **105** 165419

[214] Bian A, He D, Hao S, Fu Y, Zhang L, He J, Wang Y and Zhao H 2020 Dynamics of charge-transfer excitons in a transition metal dichalcogenide heterostructure *Nanoscale* **12** 8485–92

[215] Barre E, Dandu M, Kundu S, Sood A, da Jornada F H and Raja A 2024 Engineering interlayer hybridization in van der Waals bilayers *Nat. Rev. Mater.* **9** 499–508

[216] Chen Y, Yao W, Liu Z, Hu J, Li J and Li D 2023 Electrical control of exciton diffusion via tuning exciton states *Adv. Phys. Res.* **2** 2200083

[217] Das S, Dandu M, Gupta G, Murali K, Abraham N, Kallatt S, Watanabe K, Taniguchi T and Majumdar K 2020 Highly tunable layered exciton in bilayer WS$_2$: linear quantum confined stark effect versus electrostatic doping *ACS Photonics* **7** 5386–93

[218] Datta K, Lyu Z, Li Z, Taniguchi T, Watanabe K and Deotare P B 2022 Spatiotemporally controlled room-temperature exciton transport under dynamic strain *Nat. Photon.* **16** 242–7

[219] High A A, Novitskaya E E, Butov L V, Hanson M and Gossard A C 2008 Control of exciton fluxes in an excitonic integrated circuit *Science* **321** 229–31

[220] Andreakou P, Poltavtsev S V, Leonard J R, Calman E V, Remeika M, Kuznetsova Y Y, Butov L V, Wilkes J, Hanson M and Gossard A C 2014 Optically controlled excitonic transistor *Appl. Phys. Lett.* **104** 091101

[221] Grosso G, Graves J, Hammack A T, High A A, Butov L V, Hanson M and Gossard A C 2009 Excitonic switches operating at around 100 K *Nat. Photon.* **3** 577–80

[222] Shanks D N, Mahdikhanysarvejahany F, Koehler M R, Mandrus D G, Taniguchi T, Watanabe K, LeRoy B J and Schaibley J R 2022 Single-exciton trapping in an electrostatically defined two-dimensional semiconductor quantum dot *Phys. Rev.* B **106** L201401

[223] Shanks D N *et al* 2021 Nanoscale trapping of interlayer excitons in a 2D semiconductor heterostructure *Nano Lett.* **21** 5641–7

[224] Mak K F, Xiao D and Shan J 2018 Light-valley interactions in 2D semiconductors *Nat. Photon.* **12** 451–60

[225] Mak K F and Shan J 2016 Photonics and optoelectronics of 2D semiconductor transition metal dichalcogenides *Nat. Photon.* **10** 216–26

[226] Onga M, Zhang Y, Ideue T and Iwasa Y 2017 Exciton Hall effect in monolayer MoS_2 *Nat. Mater.* **16** 1193–7

[227] Barre E, Incorvia J A C, Kim S H, McClellan C J, Pop E, Wong H P and Heinz T F 2019 Spatial separation of carrier spin by the valley Hall effect in monolayer WSe_2 transistors *Nano Lett.* **19** 770–4

[228] Li L *et al* 2020 Room-temperature valleytronic transistor *Nat. Nanotechnol.* **15** 743–9

[229] Lagarde D, Bouet L, Marie X, Zhu C R, Liu B L, Amand T, Tan P H and Urbaszek B 2014 Carrier and polarization dynamics in monolayer MoS_2 *Phys. Rev. Lett.* **112** 047401

[230] Fang H H *et al* 2019 Control of the exciton radiative lifetime in van der Waals heterostructures *Phys. Rev. Lett.* **123** 067401

[231] Kim J *et al* 2017 Observation of ultralong valley lifetime in WSe_2/MoS_2 heterostructures *Sci. Adv.* **3** e1700518

[232] Huang Z, Liu Y, Dini K, Tan Q, Liu Z, Fang H, Liu J, Liew T and Gao W 2020 Robust room temperature valley Hall effect of interlayer excitons *Nano Lett.* **20** 1345–51

[233] Jiang C *et al* 2022 A room-temperature gate-tunable bipolar valley Hall effect in molybdenum disulfide/tungsten diselenide heterostructures *Nat. Electron.* **5** 23–27

[234] Rasmita A, Jiang C, Ma H, Ji Z, Agarwal R and W-b G 2020 Tunable geometric photocurrent in van der Waals heterostructure *Optica* **7** 1204–8

[235] Elbanna A *et al* 2023 2D material infrared photonics and plasmonics *ACS Nano* **17** 4134–79

[236] Yang S, Long H, Chen W, Sa B, Guo Z, Zheng J, Pei J, Zhan H and Lu Y 2024 Valleytronics meets straintronics: valley fine structure engineering of 2D transition metal dichalcogenides *Adv. Opt. Mater.* **12** 2302900

[237] Guo H and Qi W 2023 New materials and designs for 2D-based infrared photodetectors *Nano Res.* **16** 3074–103

[238] Zhou Y, Tan H, Sheng Y, Fan Y, Xu W and Warner J H 2018 Utilizing interlayer excitons in bilayer WS_2 for increased photovoltaic response in ultrathin graphene vertical cross-bar photodetecting tunneling transistors *ACS Nano* **12** 4669–77

[239] Lukman S *et al* 2020 High oscillator strength interlayer excitons in two-dimensional heterostructures for mid-infrared photodetection *Nat. Nanotechnol.* **15** 675–82

[240] Lopriore E, Marin E G and Fiori G 2022 An ultrafast photodetector driven by interlayer exciton dissociation in a van der Waals heterostructure *Nanoscale Horiz.* **7** 41–50

[241] Zhang K *et al* 2016 Interlayer transition and infrared photodetection in atomically thin type-II $MoTe_2/MoS_2$ van der Waals heterostructures *ACS Nano* **10** 3852–8

[242] Wang G, Li L, Fan W, Wang R, Zhou S, Lü J T, Gan L and Zhai T 2018 Interlayer coupling induced infrared response in WS_2/MoS_2 heterostructures enhanced by surface plasmon resonance *Adv. Funct. Mater.* **28** 1800339

[243] Qi T *et al* 2019 Interlayer transition in a vdW heterostructure toward ultrahigh detectivity shortwave infrared photodetectors *Adv. Funct. Mater.* **30** 1905687

[244] Afzal A M, Iqbal M Z, Dastgeer G, Nazir G and Eom J 2021 Ultrafast and highly stable photodetectors based on p-GeSe/n-$ReSe_2$ heterostructures *ACS Appl. Mater. Interfaces* **13** 47882–94

[245] Xu G, Liu D, Li S, Wu Y, Zhang Z, Wang S, Huang Z and Zhang Y 2022 Binary-ternary transition metal chalcogenides interlayer coupling in van der Waals type-II heterostructure for visible-infrared photodetector with efficient suppression dark currents *Nano Res.* **15** 2689–96

[246] Son M *et al* 2024 High-performance infrared photodetectors driven by interlayer exciton in a van der Waals epitaxy grown HfS_2/MoS_2 vertical heterojunction *Adv. Funct. Mater.* **34** 2308906

[247] Deng W *et al* 2022 Electrically tunable two-dimensional heterojunctions for miniaturized near-infrared spectrometers *Nat. Commun.* **13** 4627

[248] Zhao C, Tian W, Sun Q, Yin Z, Leng J, Wang S, Liu J, Wu K and Jin S 2020 Trap-enabled long-distance carrier transport in perovskite quantum wells *J. Am. Chem. Soc.* **142** 15091–7

[249] Kim J H, Lee J, Kim H, Yun S J, Kim J, Lee H S and Lee Y H 2019 Optical logic operation via plasmon-exciton interconversion in 2D semiconductors *Sci. Rep.* **9** 9164

[250] Xu W, Liu W, Schmidt J F, Zhao W, Lu X, Raab T, Diederichs C, Gao W, Seletskiy D V and Xiong Q 2017 Correlated fluorescence blinking in two-dimensional semiconductor heterostructures *Nature* **541** 62–67